


**Please cite the Published Version**

Gunn, Ben and Rothberg, Steve  (2025) Radial vibration measurements directly from polished-circular rotors using laser vibrometry: A new approach based on oblique incidence and retro-reflection. Mechanical Systems and Signal Processing, 225. 112238 ISSN 0888-3270

**DOI:** <https://doi.org/10.1016/j.ymssp.2024.112238>

**Publisher:** Elsevier

**Version:** Published Version

**Downloaded from:** <https://e-space.mmu.ac.uk/637846/>

**Usage rights:**  [Creative Commons: Attribution 4.0](https://creativecommons.org/licenses/by/4.0/)

**Additional Information:** This is an open access article published in Mechanical Systems and Signal Processing, by Elsevier.

**Data Access Statement:** Data will be made available on request.

**Enquiries:**

If you have questions about this document, contact [openresearch@mmu.ac.uk](mailto:openresearch@mmu.ac.uk). Please include the URL of the record in e-space. If you believe that your, or a third party's rights have been compromised through this document please see our Take Down policy (available from <https://www.mmu.ac.uk/library/using-the-library/policies-and-guidelines>)



ELSEVIER

Contents lists available at ScienceDirect

# Mechanical Systems and Signal Processing

journal homepage: [www.elsevier.com/locate/ymssp](http://www.elsevier.com/locate/ymssp)

## Radial vibration measurements directly from polished-circular rotors using laser vibrometry: A new approach based on oblique incidence and *retro*-reflection

Ben Gunn<sup>a</sup>, Steve Rothberg<sup>b,\*</sup><sup>a</sup> Formerly Wolfson School of Mechanical, Electrical and Manufacturing Engineering, Loughborough University, UK<sup>b</sup> Department of Engineering, Manchester Metropolitan University, UK

### ARTICLE INFO

Communicated by Javad Baqersad

#### Keywords:

Laser vibrometry  
 Radial  
 Rotor  
 Vibration measurement

### ABSTRACT

Laser Doppler vibrometry (LDV) offers an attractive solution when radial vibration measurement directly from a rotor surface is required. Research has demonstrated application on rough rotors (typically coated with *retro*-reflective tape) but a significant cross-sensitivity to the orthogonal radial vibration component occurs and post-processing is essential to resolve individual radial vibration components. Measurements on polished-circular rotors were then presented to overcome this problem. While these worked well, a limit on orthogonal vibration amplitude, as a proportion of laser beam diameter, was encountered, detracting from the practicality of the approach. This paper presents an alternative approach to measurements on polished-circular rotors in which incidence is switched from normal to oblique and a *retro*-reflector is incorporated into the beam path to deliver a measurement that is free from the problems encountered previously. Comprehensive theoretical and numerical analysis is presented, with experimental validation. Measurement error of around 1% was readily achieved, while cross-sensitivity to the orthogonal radial vibration component, at less than 3% for typical vibration amplitudes, was significantly lower than for alternative LDV approaches. This makes the proposed approach easily the preferred option for radial vibration measurements directly from polished-circular rotors.

### 1. Introduction

Vibration has long been acknowledged as the most effective indicator of the condition of rotating machines. Measurement and monitoring techniques are mature; the earliest significant attempts to quantify acceptable machinery vibration levels date from the late 1930s [1] and the ongoing value of vibration analysis in the diagnosis of machine health is regularly reiterated in the published literature e.g. [2–4].

Laser Doppler vibrometry (LDV) is now a mature technique [5] with commercial instruments available since the 1980s. Measurements from non-rotating parts are straightforward, provided optical access is available, with particular advantages where the context demands high frequency operation or remote transducer operation, or when the structure itself is hot or light. However, LDV also offers the opportunity to measure directly from rotating parts and measurements directly from rotating targets have been regularly highlighted by manufacturers and researchers as an important application area. Applications have been comprehensively reviewed [5–8] but new proposals and applications continue to appear in the literature covering both axial [9,10] and radial [11–15] vibration

\* Corresponding author.

<https://doi.org/10.1016/j.ymssp.2024.112238>

Received 18 May 2024; Received in revised form 9 December 2024; Accepted 12 December 2024

Available online 28 December 2024

0888-3270/© 2024 The Authors. Published by Elsevier Ltd. This is an open access article under the CC BY license (<http://creativecommons.org/licenses/by/4.0/>).

measurements. This paper is specifically concerned with the application of LDV to radial vibration measurements directly from the rotating surface, which is an application that has continued to prove problematic, as explained below.

Measurements on optically rough surfaces, including those treated with *retro*-reflective tape, are known to suffer from a significant cross-sensitivity; an *x*-radial vibration velocity measurement will exhibit a cross-sensitivity to the *y*-radial vibration *displacement* and

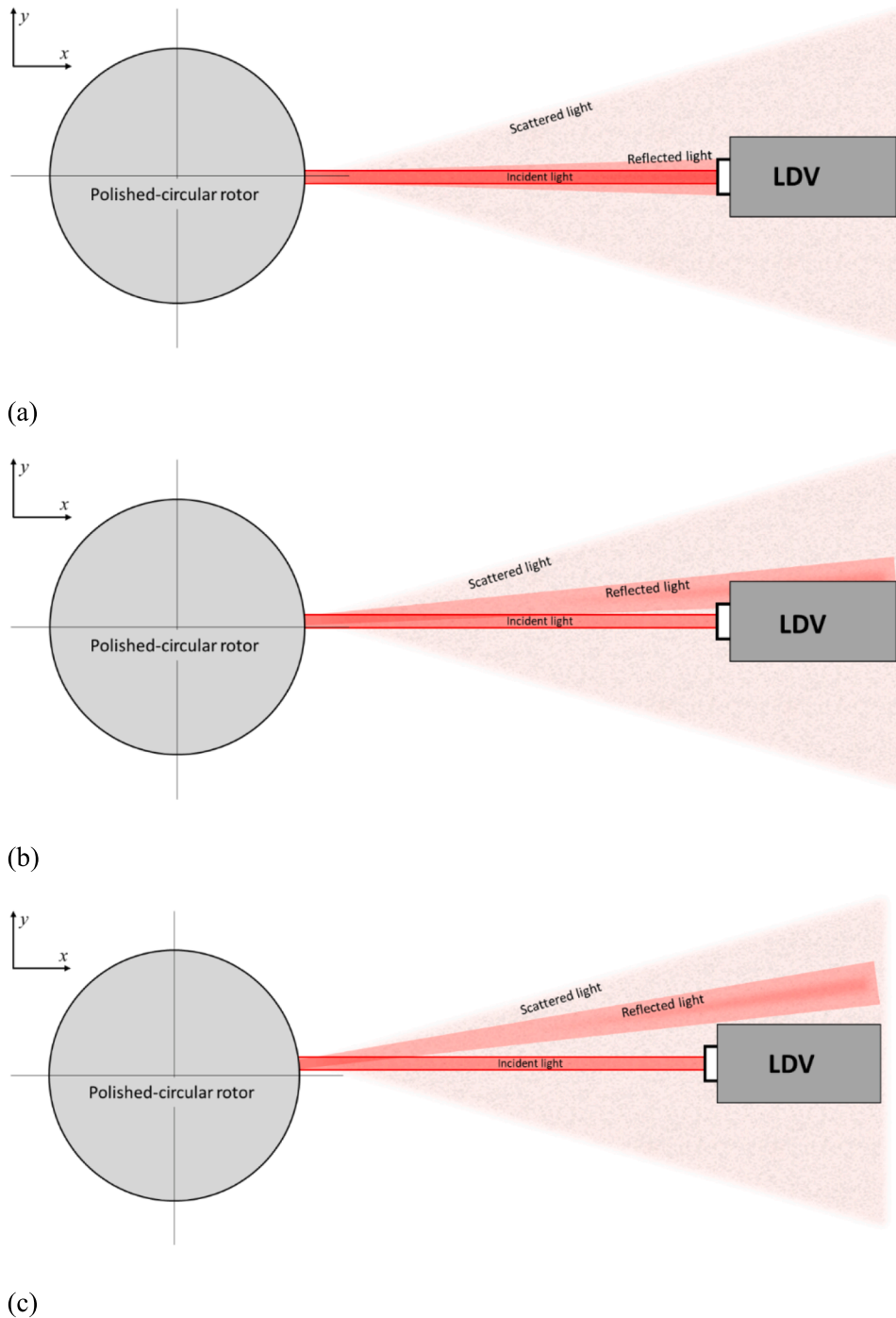


**Fig. 1.** Light collection when the LDV’s beam is incident on a polished-circular rotor (a) For zero or small *y*-radial displacement, the reflected light dominates the light collected at the aperture, (b) For larger *y*-radial displacements, the reflected and scattered light intensities collected at the aperture become comparable, (c) For *y*-radial displacements comparable with beam diameter, the scattered light intensity dominates the light collected at the aperture.

*vice-versa* [16,17]. Expressed as a percentage of the actual radial velocity, the cross-sensitivity is equal to the ratio of rotation frequency to vibration frequency, for example 100 % at the synchronous vibration frequency (vibration frequency equal to rotation frequency), 200 % at half order and 50 % at second order. As such, it cannot be ignored and a resolution procedure based on three simultaneous measurements has been formulated and must be used [18]. However, resolution at the important synchronous frequency is fundamentally not possible and typical errors close to this frequency can be problematically large [7]. Radial vibration measurements made on a polished-circular rotor (up to 50 nm surface roughness) show no such cross-sensitivity [19] but only if the radial vibration component perpendicular to the radial component it is intended to measure does not exceed an empirically obtained fraction of the incident laser beam diameter i.e. the *y*-radial vibration imposes a limit on the viability of the configuration for an *x*-radial vibration measurement and *vice-versa* [7]. It has been shown that, on rotors with surface roughness up to 10 nm, *x*-radial measurement is possible on a rotor with *y*-radial vibration displacement up to 100 % laser beam diameter, for a 90 μm beam, and up to 40 % laser beam diameter, for a 520 μm beam. On rotors with roughness between 10 nm and 50 nm, *x*-radial measurement is possible on a rotor with *y*-radial vibration displacement up to 25 % laser beam diameter, for a 90 μm beam, and only up to 10 % laser beam diameter, for a 520 μm beam. The behaviour observed is worthy of further explanation because of its relevance to the new approach proposed in this paper. It is a consequence of changes to the light collection in the presence of the orthogonal radial vibration.

For three instants, Fig. 1a-c show a simplified way of considering the light collection from a LDV's beam incident on a polished-circular rotor. Based on experience of observing the return light from surfaces with roughness from around 10 nm to a few hundred nm, each figure shows an intense specular reflection (as if from a mirrored surface) combined with a less intense background scattered light (as if from an optically rough surface with no effect from the surface curvature) in a configuration for *x*-radial measurement.

For zero or small *y*-radial displacement, the light collection at the aperture is dominated by specular reflection from the relatively intense region of the laser beam (though not necessarily its centre) that is directed along the line passing through the rotor centre, as shown in Fig. 1a. In this scenario, the absence of cross-sensitivity is a consequence of this light (directed along the line passing through the rotor centre) receiving no Doppler shift from the tangential velocity associated with whole body rotation because the laser beam and tangential velocity directions are mutually perpendicular.

However, as *y*-radial displacement increases, the collected light intensity from the specular reflection along a line passing through the rotor centre diminishes because it originates from a less intense outer part of the Gaussian-profiled incident laser beam. At some *y*-radial displacement, the dominant source of light collected becomes the diffuse scatter from all regions of the laser beam. Fig. 1b shows an instant in which reflected and scattered light intensities are broadly comparable; this would give an unreliable measurement varying between the two states. Fig. 1c shows an instant in which the scattered light dominates; the cross-sensitivity encountered in rough rotor measurements will now appear because the dominant region of the laser beam for collected light intensity is its intense geometric centre, which receives a Doppler shift from the tangential velocity associated with whole body rotation. While Fig. 1a-c show instantaneous moments, it is important to recognise that a vibration (of sufficient amplitude) results in a continuous cycle back and forth through the instants shown, all in a single measurement. While guidelines have been formulated to enable confident measurement, as outlined above, it is clear that, under such circumstances, LDV lacks the ease-of-use and versatility that users expect.

To address the usability issue for measurements on a polished-circular rotor requires an approach in which the light collected is always, even at larger orthogonal displacements, dominated by the specular reflection because this guarantees good signal strength

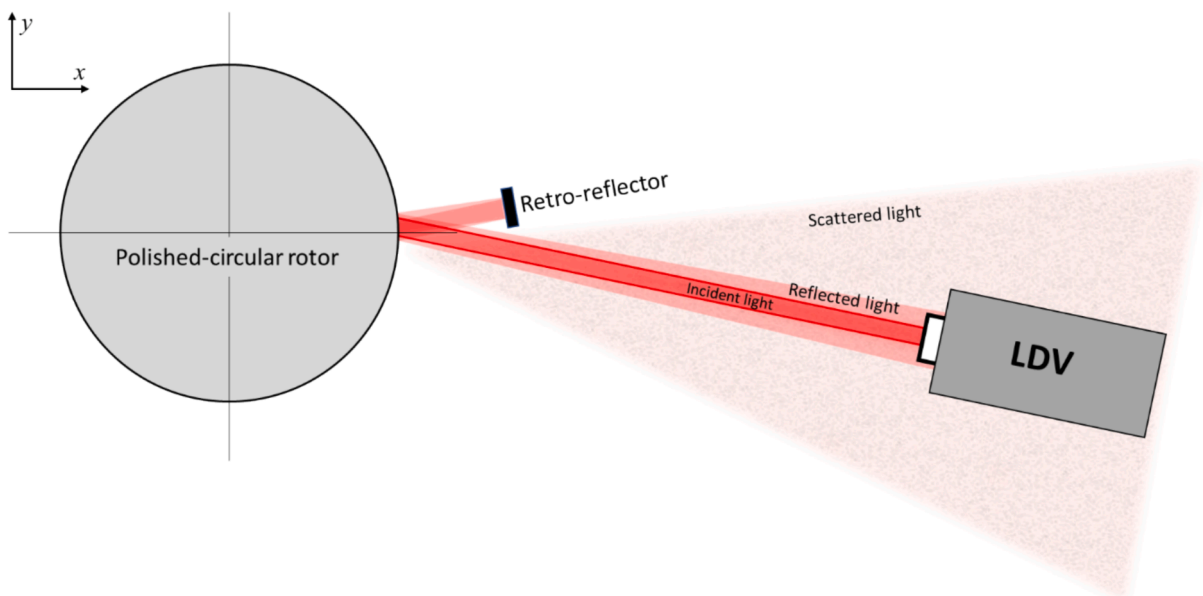


Fig. 2. Optical configuration for the proposed approach with oblique incidence and retro-reflection

but, most importantly, means the associated line of the laser beam will always have passed through the rotor centre, picking up no Doppler shift from the whole body rotation i.e. no cross-sensitivity.

A suitable configuration, incorporating a *retro*-reflecting surface or device into the optical path after oblique reflection from the target surface, was proposed recently on a vibrating polished cantilever [20] and applied subsequently to measurement from a scanning mirror [21], with the aim of overcoming loss of signal when the reflective target surface directed the return laser beam away from the LDV's collecting optics. For the rotor application, as shown in Fig. 2, the advantages extend beyond simply maintaining signal strength. With oblique incidence, the light is reflected from the rotor surface and away from the optical head of the instrument. The retroreflector returns that light along the same path to a second reflection on the rotor surface and from there along the same path as the original incident laser beam such that the bright centre of the returning laser beam is automatically centred on the collecting aperture. The double reflection gives the added benefit of doubled sensitivity, more than compensating for the slight reduction in sensitivity associated with oblique incidence.

This paper explores the use of this configuration with novel elements as follows. The principle of the proposed approach is set out mathematically, for arbitrary target motion and beam alignment. Numerical analysis of specific scenarios then enables exploration of the main measurement errors and any cross-sensitivities to demonstrate how the approach overcomes the limitations of normal incidence measurements on a polished-circular rotor. First-time experiments are then conducted to confirm the practical viability of the approach, including the mathematical prediction of sensitivity with associated errors and cross-sensitivities placed in the context of real measurements. Finally, the effect of inevitable laser beam misalignments is presented through numerical simulation to confirm in greater depth the viability of the approach.

## 2. Modelling the measured velocity

### 2.1. Comparing the normal and oblique incidence configurations

The modelling framework used here [6] starts with the fundamental relationship between measured velocity,  $U_m$ , and surface velocity at any measurement point  $P$ ,  $\vec{V}_P$ , which is captured in the expression:

$$U_m = \frac{1}{2}(\hat{b}_2 - \hat{b}_1) \cdot \vec{V}_P \quad (1)$$

in which  $\hat{b}_2$  and  $\hat{b}_1$  are, respectively, unit vectors for the laser beam directions immediately after and immediately before the point  $P$ . Equation (1) can be applied to normal and oblique incidence at a target surface. For normal incidence, as in Fig. 1 a-c, and light collected in retroreflection,  $\hat{b}_2 = -\hat{b}_1 = \hat{n}_P$ , where  $\hat{n}_P$  is the surface normal unit vector at the point  $P$ , and equation (1) simplifies to:

$$U_m = \hat{n}_P \cdot \vec{V}_P \quad (2)$$

This represents the LDV configuration commonly used and means the measured velocity is the component in the direction of the surface normal at the incident point  $P$ . Since the rotor is polished and circular, that surface normal passes through the rotor centre as required to prevent the cross-sensitivity associated with rotational velocity.

For oblique incidence, reflection from the rotor surface, retroreflection from an additional (stationary) surface or device, and return along the same path, as shown in Fig. 2, the laser beam frequency is shifted at both encounters with the rotor so that the measured velocity is given by:

$$U_m = \frac{1}{2}(\hat{b}_2 - \hat{b}_1) \cdot \vec{V}_P + \frac{1}{2}(-\hat{b}_1 - \hat{b}_2) \cdot \vec{V}_P = (\hat{b}_2 - \hat{b}_1) \cdot \vec{V}_P \quad (3a)$$

For reflections, the incident and reflected beam orientations are related by

$$\hat{b}_2 - \hat{b}_1 = -2(\hat{b}_1 \cdot \hat{n}_P)\hat{n}_P \quad (3b)$$

and so the measured velocity can be written as:

$$U_m = -2(\hat{b}_1 \cdot \hat{n}_P)\hat{n}_P \cdot \vec{V}_P \quad (4)$$

Equation (4) shows that, for any laser Doppler configuration with an incoming and a reflected beam, there is sensitivity to velocity in the direction of the surface normal at the point of incidence which is also, through the law of reflection, the direction of the bisector between incident and reflected beams. Importantly, this is exactly the same as the component measured with the normal incidence LDV configuration, as seen in equation (2). Furthermore, Equation (4) shows a possible doubling in sensitivity, compared to the normal incidence configuration to which equation (2) applies. While the physical space requirement prevents exact alignment between  $\hat{b}_1$  and  $\hat{n}_P$ , an angle between the two of  $15^\circ$ , for example, would still give 1.93 times the sensitivity for the oblique incidence LDV configuration compared to the normal incidence LDV configuration.

### 2.2. Advantages of the oblique incidence configuration for the rotor application

Increased sensitivity is always welcome but there are two much more important advantages of the alternative configuration that are

specific to the application to radial vibration measurement on a polished-circular rotor.

Firstly, because the retroreflection guarantees that the path after the second reflection on the rotor will follow the line of the incident laser beam from the outgoing path, the central (most intense) region of the returning laser beam will always dominate the light collection; thus, the problem with the normal incidence measurement associated with dominance of the diffusely scattered light at greater vibration displacements is overcome. Practically, this removes the limitation on tolerable orthogonal vibration displacement, related to beam diameter, encountered in the normal incidence measurement approach [7].

Secondly, the surface normal for a circular rotor will, by definition, always pass through the rotor centre, which is the essential requirement for radial vibration measurements free from the cross-sensitivity to velocity associated with target rotation encountered in rough rotor measurements [7]. This can be seen mathematically by expressing the surface velocity at the point of interest,  $P$ , on a structure as the sum of a translational velocity,  $\vec{V}_O$ , of a reference point,  $O$ , fixed in the structure and the velocity of the point of interest relative to that reference point, as a result of rotation about an instantaneous rotation axis passing through the reference point, at angular velocity  $\vec{\omega}$ . For the incident point  $P$  and the reference point  $O$ :

$$\vec{V}_P = \vec{V}_O + \vec{\omega} \times \vec{OP} \tag{5a}$$

However, there is no dependence on  $\vec{\omega}$  in the measured velocity because of the co-dependence on the surface normal. The mathematical expression shows this readily as:

$$\hat{n}_P \cdot \vec{V}_P = \hat{n}_P \cdot \vec{V}_O + \hat{n}_P \cdot (\vec{\omega} \times \vec{OP}) \tag{5b}$$

The final term of equation (5b) always evaluates to zero because  $\hat{n}_P$  and  $\vec{OP}$  are inherently parallel for a rotor with a circular cross-section. Consequently, equation (4) is refined to:

$$U_m = -2(\hat{b}_1 \cdot \hat{n}_P) \hat{n}_P \cdot \vec{V}_O \tag{6}$$

which means that the measured velocity is unaffected by target rotation and can be conveniently thought of as the appropriate component of the velocity of the centre ( $O$ ) of the axial element on which the beam is incident.

### 2.3. Laser beam orientation

To achieve the desired measurement requires the laser beam to be incident at a point on the rotor where the surface normal is

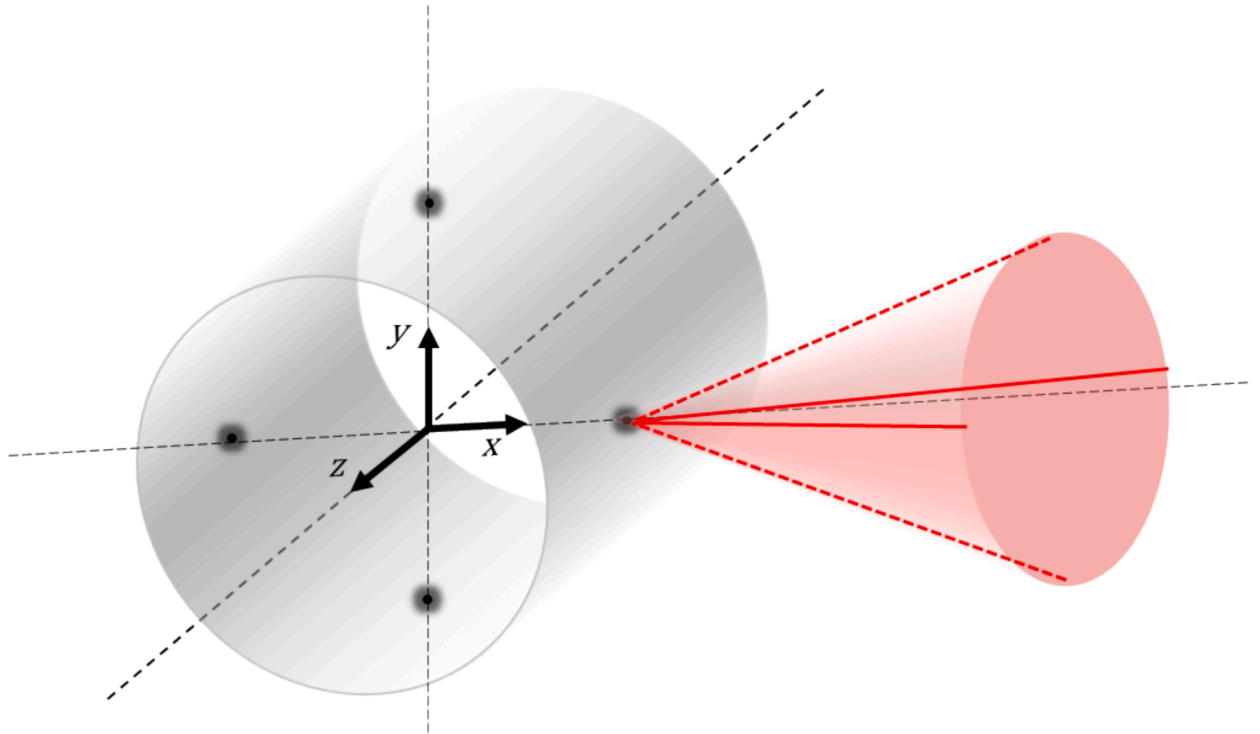


**Fig. 3.** Possible incident beam orientations for x-radial vibration measurements lie anywhere in the surface of a cone whose apex is at a point on the rotor through which its x-axis passes.

orientated in the direction of the motion component it is intended to measure. For example, to measure  $x$ -radial velocity requires incidence at a point on the rotor through which its  $x$ -axis passes but the orientation of the incident beam can be anywhere in the surface of a cone whose apex is at the measurement point. This means that the reflected beam will also lie in the surface of the same cone, as shown in Fig. 3. Whatever the orientation, the angle of incidence,  $\theta$ , is half the cone's apex angle such that:

$$U_m \approx 2\cos\theta \hat{n}_p \cdot \vec{V}_O' \tag{7}$$

The approximate nature of equation (7) acknowledges slight changes in the incident point  $P$  during vibration which cause  $(\hat{b}_1 \cdot \hat{n}_p)$  to be slightly time dependent. While this approximation is confirmed as acceptable in sub-section 3.1, this time dependence is the main source of error and cross-sensitivity for the proposed approach since  $\hat{n}_p$  sets the actual sensitivity axis for any measurement and its time dependence, albeit small, makes it differ from the intended sensitivity direction,  $x$ , which is fixed. This is also introduced in sub-section 3.1 and then explored numerically through the rest of section 3 and experimentally in section 4.

The apex angle must be large enough to allow incorporation of the retro-reflecting surface or device into the configuration but keeping the angle small ensures higher sensitivity. In Fig. 3, for illustrative purposes and to make a link to later stages of the paper, an incident / reflected beam combination is shown (as solid lines) in the  $xz$  (horizontal) plane and a second beam combination is shown (as dashed lines) in the  $xy$  (vertical) plane.

Equation (6) shows that the measured velocity depends on the beam orientation, which is constant, and the point of incidence, from which both the surface velocity and the surface normal direction follow. A feature of non-contact measurement compared to use of contacting transducers is small variation in the exact location of the measurement point on the structure as the structure vibrates. If it is found that this small variation has no consequence, the measurements are made according to equation (7) but previous research for measurements on rough rotors has shown how these same changes in the location of the incident beam result in a significant cross-sensitivity. Therefore, the next sub-section sets out how to find the precise point of incidence.

#### 2.4. Identifying the point of incidence

Fig. 4 shows a schematic diagram of a measurement on a circular rotor, radius  $R$ . Three axial elements are shown. The first (solid black line) is the element on which the laser beam (without misalignments) is incident in the absence of vibration; it is centred at  $O$  and the laser beam is incident at point  $B$  where the surface normal is aligned with the  $x$ -axis such that:

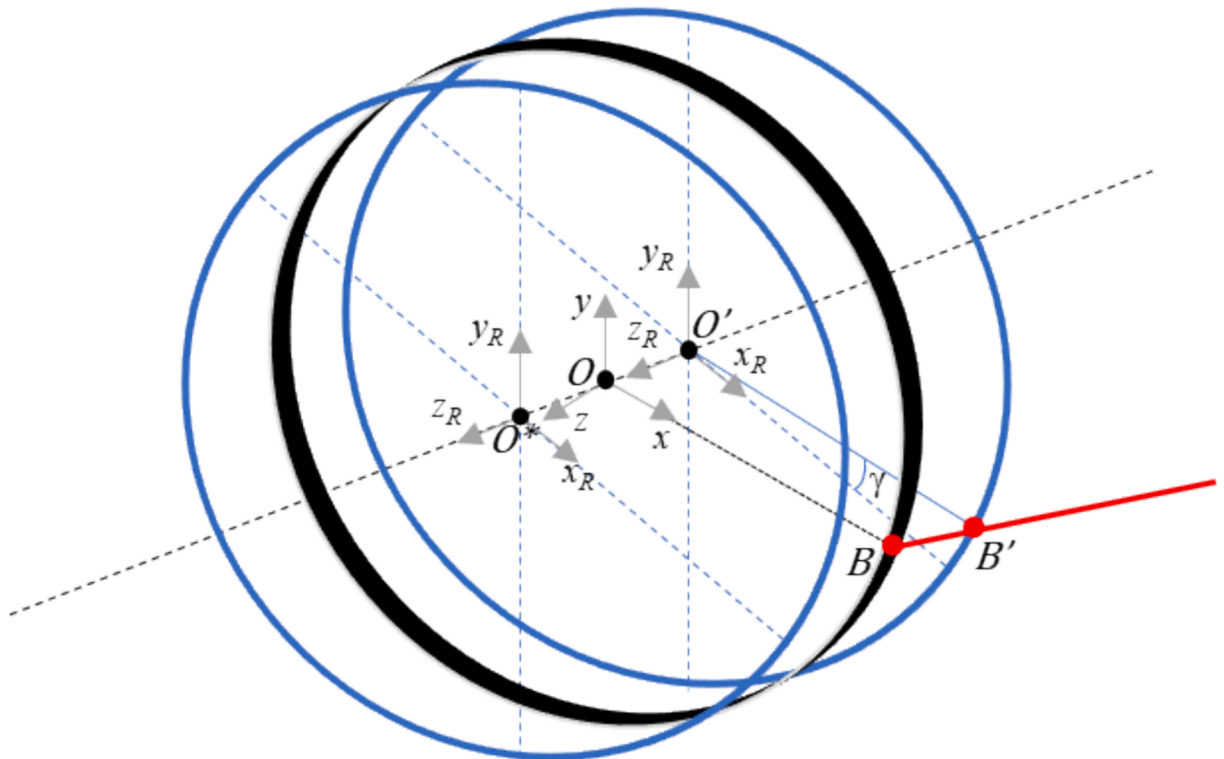


Fig. 4. Laser beam incidence on the polished-circular rotor showing the illuminated point,  $B$ , before vibration displacement (black axial element, centre  $O$ ), the new position of that axial element after angular and translational vibration displacement (front blue axial element, centre  $O^*$ ) and the parallel axial element now illuminated by the laser beam at point  $B'$  as a result of that vibration displacement (rear blue axial element, centre  $O'$ ). (For interpretation of the references to colour in this figure legend, the reader is referred to the web version of this article.)



$$\overrightarrow{OB} = R\hat{x} \tag{8a}$$

$$\hat{n}_B = \hat{x} \tag{8b}$$

The displaced position of this axial element, as a result of arbitrary translational and angular displacements, is also shown (front axial element, solid blue line), centred at point  $O^*$ . The instantaneous translational vibration displacement is  $\overrightarrow{OO^*}$  and the instantaneous angular vibration displacements are  $\alpha$  and  $\beta$ . This axial element centred at  $O^*$  has local axes related to the global coordinates through  $\alpha$  and  $\beta$  as follows:

$$[\hat{x}_R \ \hat{y}_R \ \hat{z}_R] = [\hat{x} \ \hat{y} \ \hat{z}][x, \alpha][y, \beta] \begin{bmatrix} 1 & 0 & 0 \\ 0 & 1 & 0 \\ 0 & 0 & 1 \end{bmatrix} \tag{9}$$

where  $[x, \alpha]$  and  $[y, \beta]$  are rotation matrices as stated in [Appendix A](#). The laser beam is now incident at point  $B'$  on another axial element (rear axial element, solid blue line) that is centred at  $O'$  and parallel to the displaced element containing  $O^*$ . Assuming the short axial extent of the rotor that is illuminated behaves as a rigid body, finding the location of  $B'$  is achieved by expressing its position from rotor and laser beam perspectives. Starting with the rotor perspective, the location of  $B'$  can be written as:

$$\overrightarrow{OB'} = \overrightarrow{OO^*} + \overrightarrow{O^*O'} + \overrightarrow{O'B'} \tag{10}$$

The axial elements containing  $O^*$  and  $O'$  have a small (and as yet unknown) axial separation  $Z'$  which is written as:

$$\overrightarrow{O^*O'} = Z'\hat{z}_R \tag{11}$$

Within its axial element,  $\overrightarrow{O'B'}$  can be conveniently written as a radius vector with a small (and as yet unknown) angular separation,  $\gamma$ , from the  $\hat{x}_R$ -direction:

$$\overrightarrow{O'B'} = [\hat{x}_R \ \hat{y}_R \ \hat{z}_R][z, \gamma][R \ 0 \ 0]^T \tag{12}$$

From the laser beam perspective, the position of  $B'$  is written in terms of any known point on the incident laser beam,  $A$ , and the laser beam orientation,  $\hat{b}_1$ .

$$\overrightarrow{OB'} = \overrightarrow{OA} + p\hat{b}_1 \tag{13}$$

where  $p = |\overrightarrow{BB'}|$  is also as yet unknown. For a laser beam with perfect alignment, and without any loss of generality, the point  $B$  is a good choice for the known point such that:

$$\overrightarrow{OA} = \overrightarrow{OB} = R\hat{x} \tag{14a}$$

With misalignments, the laser beam no longer passes through point  $B$  but shifts to pass through a point that can be thought of as being in the same  $yz$ -plane as  $B$  but with translational misalignments in the  $y$ - and  $z$ -direction of  $\Delta y_A$  and  $\Delta z_A$ , respectively:

$$\overrightarrow{OA} = R\hat{x} + [\hat{x} \ \hat{y} \ \hat{z}][0 \ \Delta y_A \ \Delta z_A]^T \tag{14b}$$

Angular orientation and misalignments are incorporated into the laser beam orientation,  $\hat{b}_1$ , using rotation matrices. For example, for an initial orientation in the negative  $x$ -direction, followed by rotations  $\beta_L$  and  $\alpha_L$  around  $y$ - and  $x$ -axes respectively, the final orientation is given by:

$$\hat{b}_1 = [\hat{x} \ \hat{y} \ \hat{z}][x, \alpha_L][y, \beta_L][-1 \ 0 \ 0]^T \tag{15}$$

Later analysis refers to an  $xz$  plane arrangement and  $xy$  plane arrangement. In equation (15), the  $xz$ -plane arrangement requires only a rotation around the  $y$ -axis,  $\beta_L = \theta$ , while the  $xy$ -plane arrangement requires the same rotation around the  $y$ -axis,  $\beta_L = \theta$ , followed by rotation around the  $x$ -axis,  $\alpha_L = \pi/2$  rad. The angles  $\beta_L$  and  $\alpha_L$  can include both the desired orientation and any angular error.

Finding  $\overrightarrow{OB'}$  proceeds by combining equations (10) to (13) and separating terms in the rotor's local coordinate system from terms more easily written in the global coordinates, which gives:

$$Z'\hat{z}_R + [\hat{x}_R \ \hat{y}_R \ \hat{z}_R][z, \gamma][R \ 0 \ 0]^T = \overrightarrow{OA} + p\hat{b}_1 - \overrightarrow{OO^*} \tag{16}$$

Equation (16) has three unknowns,  $Z$ ,  $\gamma$  and  $p$ , and these can be found (for any state of alignment and arbitrary vibration) by applying the coordinate transformation in equation (9). As derived in [Appendix B](#), the left hand side of equation (16), rewritten more concisely in the rotor's local coordinate system, can be expressed in the global coordinates as:



$$\begin{bmatrix} \hat{x}_R & \hat{y}_R & \hat{z}_R \end{bmatrix} \begin{bmatrix} R \cos \gamma \\ R \sin \gamma \\ Z \end{bmatrix} = \begin{bmatrix} \hat{x} & \hat{y} & \hat{z} \end{bmatrix} \begin{bmatrix} R \cos \gamma \cos \beta + Z \sin \beta \\ R \cos \gamma \sin \beta + R \sin \gamma \cos \alpha - Z \sin \alpha \cos \beta \\ -R \cos \gamma \cos \alpha \sin \beta + R \sin \gamma \sin \alpha + Z \cos \alpha \cos \beta \end{bmatrix} \quad (17)$$

Equating corresponding dimensions of the right hand sides of equation (17) and equation (16) provides the 3 equations required to solve for  $Z$ ,  $\gamma$  and  $p$ :

$$R \cos \gamma \cos \beta + Z \sin \beta = R + p b_{1x} - (\overline{OO^*})_x \quad (18a)$$

$$R \cos \gamma \sin \beta + R \sin \gamma \cos \alpha - Z \sin \alpha \cos \beta = \Delta y_A + p b_{1y} - (\overline{OO^*})_y \quad (18b)$$

$$-R \cos \gamma \cos \alpha \sin \beta + R \sin \gamma \sin \alpha + Z \cos \alpha \cos \beta = \Delta z_A + p b_{1z} - (\overline{OO^*})_z \quad (18c)$$

in which  $b_{1x}$ ,  $b_{1y}$  and  $b_{1z}$  are the magnitudes of the  $x$ ,  $y$  and  $z$  components of  $\hat{b}_1$ , and  $(\overline{OO^*})_x$ ,  $(\overline{OO^*})_y$  and  $(\overline{OO^*})_z$  are the instantaneous magnitudes of the  $x$ ,  $y$  and  $z$  components of  $\overline{OO^*}$ . Solution of these equations allows location of  $B'$  from equation (10) or (13).

Solution also requires expression of the surface normal vector based on equation (12):

$$\hat{n}_B = \frac{\overline{OB'}}{R} = \begin{bmatrix} \hat{x}_R & \hat{y}_R & \hat{z}_R \end{bmatrix} [z, \gamma] \begin{bmatrix} 1 & 0 & 0 \end{bmatrix}^T = \cos \gamma \hat{x}_R + \sin \gamma \hat{y}_R \quad (19a)$$

Using the coordinate transformation from [Appendix B](#) allows expansion of this vector as:

$$\hat{n}_B = \cos \gamma \cos \beta \hat{x} + (\cos \gamma \sin \beta \sin \alpha + \sin \gamma \cos \alpha) \hat{y} - (\cos \gamma \cos \alpha \sin \beta - \sin \gamma \sin \alpha) \hat{z} \quad (19b)$$

The manipulation of equations (18a-c) is algebraically lengthy and not shown here but, in [sub-section 3.2](#) supplemented by [Appendix C](#), minor simplifications to equations (18a-c) make solution for  $Z$ ,  $\gamma$  and  $p$  much easier to show, without compromising the need to explore the viability of the proposed approach.

### 3. Numerical assessment

All of the data in this section result from a numerical analysis using the equations derived theoretically in [section 2](#). For each scenario, a full rotation period of measured data is calculated from which errors and cross-sensitivities are evaluated in two forms. The first is the instantaneous form set out in [sub-section 3.1](#), supplemented by the RMS over a cycle. The second form is based on the magnitudes of spectral peaks at frequencies of interest. In each scenario, the 'true' velocity or magnitude is known because it is an input to the numerical analysis.

#### 3.1. Expressing instantaneous measurement error and cross-sensitivity

Measurement error follows a standard definition of the difference between true and measured velocity as a proportion of the true velocity. It can, of course, be written for any intended measurement but, since this paper is concerned with radial vibration measurements, the  $x$ -radial component,  $V_{Ox}$ , is chosen here and will then be used throughout the remainder of the paper. Looking back at equation (6), the desired measurement can be written as  $-2b_{1x}V_{Ox}$  and the instantaneous measurement error,  $IE$ , is then conveniently written as:

$$IE = 1 - \frac{U_m}{-2b_{1x}V_{Ox}} \quad (20)$$

When the effect of vibration other than in the direction of the intended measurement is to be assessed, especially in the absence of vibration in the intended measurement direction, an instantaneous cross-sensitivity,  $ICS$ , can be calculated by taking the measured velocity, dividing by  $-2b_{1x}$  to scale, and then dividing by the instantaneous velocity,  $V_{CS}$ , to which cross-sensitivity is being calculated:

$$ICS = \frac{U_m}{-2b_{1x}V_{CS}} \quad (21)$$

Before focussing on simpler target motion, sources of measurement error for arbitrary target motion will be considered briefly. Using small angle approximations, and then neglecting double angles, equations (19b) and (6) simplify as follows:

$$\hat{n}_B \approx \hat{x} + \gamma \hat{y} - \beta \hat{z} \quad (22)$$

$$U_m \approx -2b_{1x}V_{Ox} - 2(\gamma b_{1y} - \beta b_{1z})V_{Ox} - 2\gamma b_{1x}V_{Oy} + 2\beta b_{1x}V_{Oz} \quad (23)$$

in which  $V_{Ox}$ ,  $V_{Oy}$  and  $V_{Oz}$  are the instantaneous magnitudes of the  $x$ ,  $y$  and  $z$  components of  $\overline{VO}$ . The instantaneous error, according

to equation (20), is then written as:

$$IE \approx \frac{-\gamma b_{1y}}{b_{1x}} + \frac{\beta b_{1z}}{b_{1x}} - \frac{\gamma V_{Oy}}{V_{Ox}} + \frac{\beta V_{Oz}}{V_{Ox}} \tag{24}$$

Inspection of equation (24) shows that there are four main error terms in an  $x$ -radial vibration measurement on a rotor with arbitrary vibration. The first is especially important because it occurs even when the vibration is limited to the single component that it is intended to measure. The three further error terms are all the result of other vibration components, including some cross-sensitivity to the angular vibration around the  $y$ -axis (yaw),  $\beta$ , and the  $y$ -radial and axial vibrations,  $V_{Oy}$  and  $V_{Oz}$ . All the errors will be small if the angles  $\gamma$  and  $\beta$  are small. For  $\beta$ , this is a reasonable assumption, while for  $\gamma$  this will be confirmed in the calculations performed in sub-section 3.2. Thus, equation (24) finally confirms that the approximation in equation (7) is acceptable.

There is, however, a limitation on the quantitative use of equation (24); the final 2 terms can give rise to large individual values when  $V_{Ox}$  is instantaneously zero (when  $V_{Oy}$  or  $V_{Oz}$  is not). Consequently, equation (24) is helpful to identify primary sources of measurement error but is only reliable to use quantitatively when  $V_{Ox}$  is the sole motion, which is unlikely in practice.

### 3.2. Measurement scenarios

The scale of the angle,  $\gamma$ , is clearly a significant factor for this approach and attention is now turned to calculation of typical values, firstly to confirm that  $\gamma$  is indeed small but mainly to quantify the consequent error in a measurement of  $x$ -radial vibration and the consequent cross-sensitivity to  $y$ -radial vibration in an  $x$ -radial measurement because these matters are central to the viability of the proposed method.

Using small angle approximations for  $\alpha$  and  $\beta$  and neglecting their double angles are relatively minor approximations that significantly simplify solution of equations (18a-c). These equations can also be written in a convenient form, normalised to the rotor radius, as:

$$\cos\gamma \approx 1 + \left(\frac{P}{R}\right)b_{1x} - \left(\frac{Z}{R}\right)\beta - \frac{(\overline{OO^z})_x}{R} \tag{25a}$$

$$\sin\gamma \approx \frac{\Delta y_A}{R} + \left(\frac{P}{R}\right)b_{1y} + \left(\frac{Z}{R}\right)\alpha - \frac{(\overline{OO^z})_y}{R} \tag{25b}$$

$$\left(\frac{Z}{R}\right) \approx \frac{\Delta z_A}{R} + \left(\frac{P}{R}\right)b_{1z} - \frac{(\overline{OO^z})_z}{R} + \beta \cos\gamma \tag{25c}$$

Analytical solution of equations (25a-c) can be performed readily for all the scenarios considered in the next sub-sections. In all cases, the angle of incidence,  $\theta = 15^\circ$ . Solutions are detailed in Appendix C to keep the main narrative clear.

#### 3.2.1. Measurement error due to $x$ -radial vibration for $x$ -radial vibration measurement in $xy$ -plane configuration

In this first scenario, the laser beam orientation is in the  $xy$ -plane, as shown in side-view in Fig. 5. The Figure shows how the  $x$ -

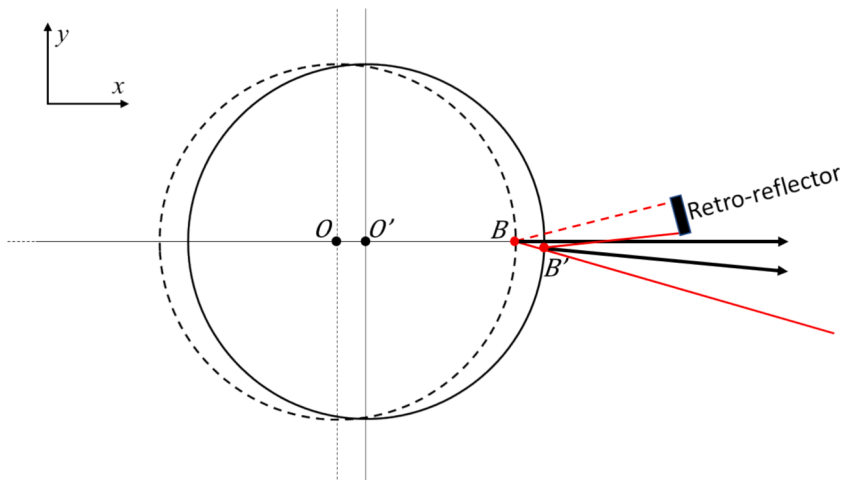


Fig. 5. Change in the point of laser beam incidence and in the surface normal unit vector due to  $x$ -radial vibration displacement in an  $x$ -radial measurement with  $xy$ -plane arrangement.

vibration of the target causes a small and continuous deviation in the direction of the surface normal away from the  $x$ -direction. This will cause an error that will be quantified numerically in this sub-section. Note that the deviation of the beam is exaggerated in the figure for clarity. (In the experiments described later, the movement of the beam on the *retro*-reflector was estimated as up to 1 mm).

Fig. 6a shows one rotation period of simulated measured vibration velocity from sinusoidal  $x$ -radial displacements with amplitudes 0.01R and 0.1R and frequency equal to rotation frequency. It is shown in a convenient normalised form and serves to confirm, ahead of more rigorous quantitative analysis, that a faithful representation of the target motion is provided. These two displacement amplitudes are chosen throughout this sub-section for illustrative purposes, with the general intention of indicating a range from modest (0.01R) to extreme (0.1R) vibration displacements [1]. Equation (24) showed how the angle  $\gamma$  drives measurement error. As set out in Appendix C, equations (25a-c) show  $Z = 0$  throughout the cycle and they also reveal the behaviour of  $\gamma$  as shown in Fig. 6b. The values confirm the small angle assumption for  $\gamma$ , as used in equations (22) and (23), is reasonable. Growth in the angle  $\gamma$  is a direct result of the movement in the point of incidence, as shown in Fig. 5, which clearly amplifies for larger displacement amplitude. This causes deviation of the surface normal direction, with a consequent instantaneous error in the form of equation (C6).

Though not easily visible in Fig. 6b, the values of  $\gamma$  at each end of the vibration cycle differ very slightly and this causes a corresponding asymmetry in the instantaneous error, which is more readily visible in Fig. 7a:  $-0.64\%$  at  $(\overrightarrow{OO^*})_x = 0.1R$  and  $0.79\%$  at  $(\overrightarrow{OO^*})_x = -0.1R$ . The practical implication of the asymmetry is minimal though, as a harmonic distortion, it does mean that a single frequency vibration will cause small errors that appear at integer multiples of that frequency. The instantaneous error plot shows how this is driven by (i.e. is in phase with) displacement, rather than velocity. This means that instantaneous error is largest when velocity is small. The RMS of the instantaneous error, as shown in Fig. 7b, shows growth in direct proportion to vibration amplitude as well as tolerably small values even at the extreme displacement.

The RMS value is a useful quantity to consider when evaluating the proposed approach but a visual comparison of the actual and measured velocity, as shown in Fig. 7c, confirms such close agreement between actual (grey solid line) and measured (superimposed dashed black line) velocities that the two are indistinguishable, even for the larger vibration displacement amplitude of 0.1R. As indicated at the end of sub-section 3.1, this RMS calculation is affected by large instantaneous error values occurring at the smallest velocities, exaggerating the measurement error.

For this reason, a calculation is also made of the magnitude of the spectral peak at the vibration frequency, following the standard way in which error would be evaluated from experimental data. A Magnitude Error can then be calculated as the difference between the true magnitude and the measured magnitude (at the same frequency) normalised by the true magnitude. This is shown in Fig. 7d. Even though the rate of growth of this error increases with increasing vibration amplitude, at  $<0.02\%$  it remains truly negligible across the full vibration amplitude range considered.

### 3.2.2. Measurement error due to $x$ -radial vibration for $x$ -radial vibration measurement in $xz$ -plane configuration

Though already small, it is possible to reduce this error to zero with a simple change of incident beam geometry. In sub-section 2.3, it was explained that the incident laser beam can sit anywhere in the surface of a cone whose apex is at the incident point and whose axis is aligned with the surface normal. The measured velocity component is the same in all orientations. Fig. 8 shows a plan-view of the rotor with the laser beam now incident, and subsequently reflected, in the  $xz$ -plane. In this orientation, an  $x$ -radial displacement of the rotor causes an axial shift in the point of incidence but no change in the direction of the surface normal and, so,  $\gamma$  remains zero. This is apparent in Fig. 8 and, because  $b_{1y} = 0$  and  $(\overrightarrow{OO^*})_y = 0$  for this second scenario, is also easily confirmed by equation (25b).

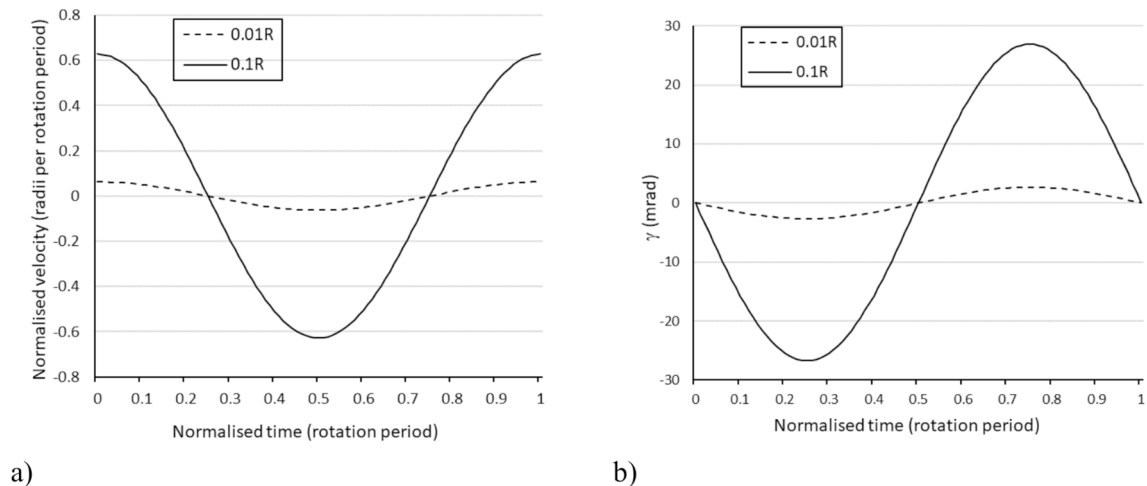
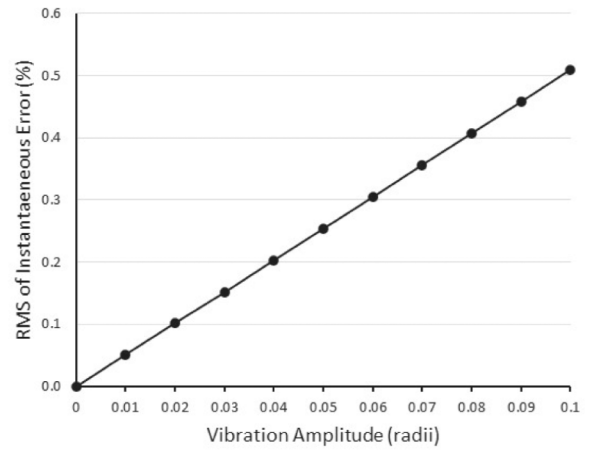
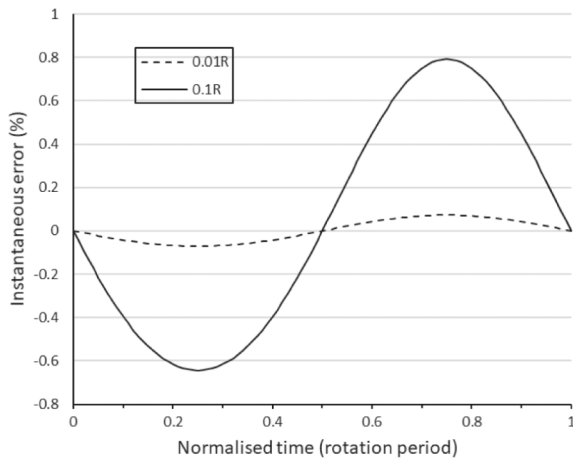
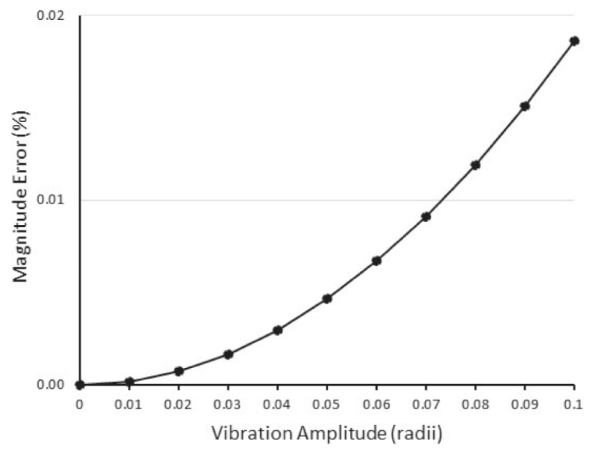
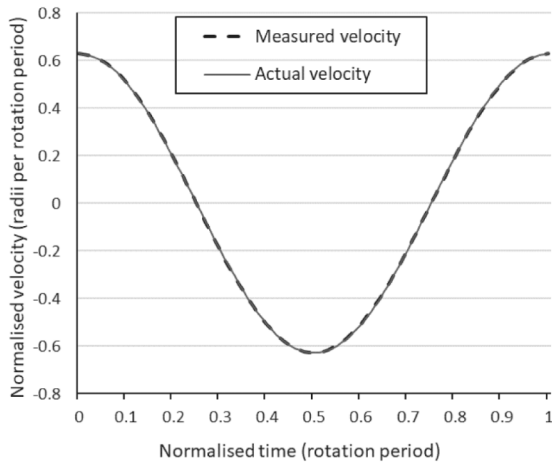


Fig. 6. Simulated  $x$ -radial vibration measurement on a rotor with  $x$ -radial vibration only and with laser beam incidence in the  $xy$ -plane a) Normalised velocity measurement b) Angle  $\gamma$



a)

b)



c)

d)

**Fig. 7.** Error in a simulated x-radial vibration measurement on a rotor with x-vibration only and with laser beam incidence in the xy plane a) Instantaneous error through the vibration cycle b) RMS of the instantaneous error as a function of vibration amplitude c) Visual comparison of the actual and measured velocity for a vibration displacement amplitude of 0.1R d) Magnitude Error as a function of vibration amplitude.

Fig. 9a shows a rotation period of simulated measured vibration velocity from sinusoidal displacements with amplitudes 0.01R and 0.1R and frequency equal to twice rotation frequency. The change in vibration frequency is just for variety and illustrative purposes. As set out in Appendix C, the shift in the illuminated axial element scales to the vibration displacement by the tan of the incident angle (0.268 for 15° incidence), as shown in Fig. 9b, but most importantly the associated error is zero at all times because  $\gamma = 0$  irrespective of vibration displacement.

The variation in the RMS of the instantaneous error due to orientation of the incident laser beam around the surface of the cone (see Fig. 3) is shown in Fig. 10a. Orientation is defined here with reference to equation (15) in which laser beam orientation is set by an initial alignment in the negative x-direction, followed by a fixed rotation around the y-axis,  $\beta_L = -15^\circ$ , followed by increments in rotation  $\alpha_L$ , around the x-axis. The x-radial measurement error increases from zero with laser beam incidence in the xz-plane ( $\alpha_L = 0^\circ$ ) to a maximum when the laser beam is incident in the xy-plane ( $\alpha_L = 90^\circ$ ) and then decreases again as the incident beam orientation rotates back around into the xz-plane ( $\alpha_L = 180^\circ$ ), where it is zero again. This repeats for continued rotation up to  $360^\circ$ . The error is driven by the angle  $\gamma$ , which is shown in Fig. 10b. An RMS of the instantaneous error of 0.51 % was calculated for the extreme amplitude of 0.1R and 15° angle of incidence, so all orientations produce accurate measurements but orientation in the xz plane is optimum and this numerical analysis suggests it should be the default option.

The downside of orientation in the xz-plane, compared to orientation in the xy-plane, is error associated with the angular vibration  $\beta$ , according to the second and fourth terms in equation (24). Values as calculated for  $\gamma$  above and typical values for  $\beta$  are likely to be of similar magnitude, so it is possible that any benefit of the orientation in the xz-plane through minimising the ' $\gamma b_{1y}$ ' error might be lost

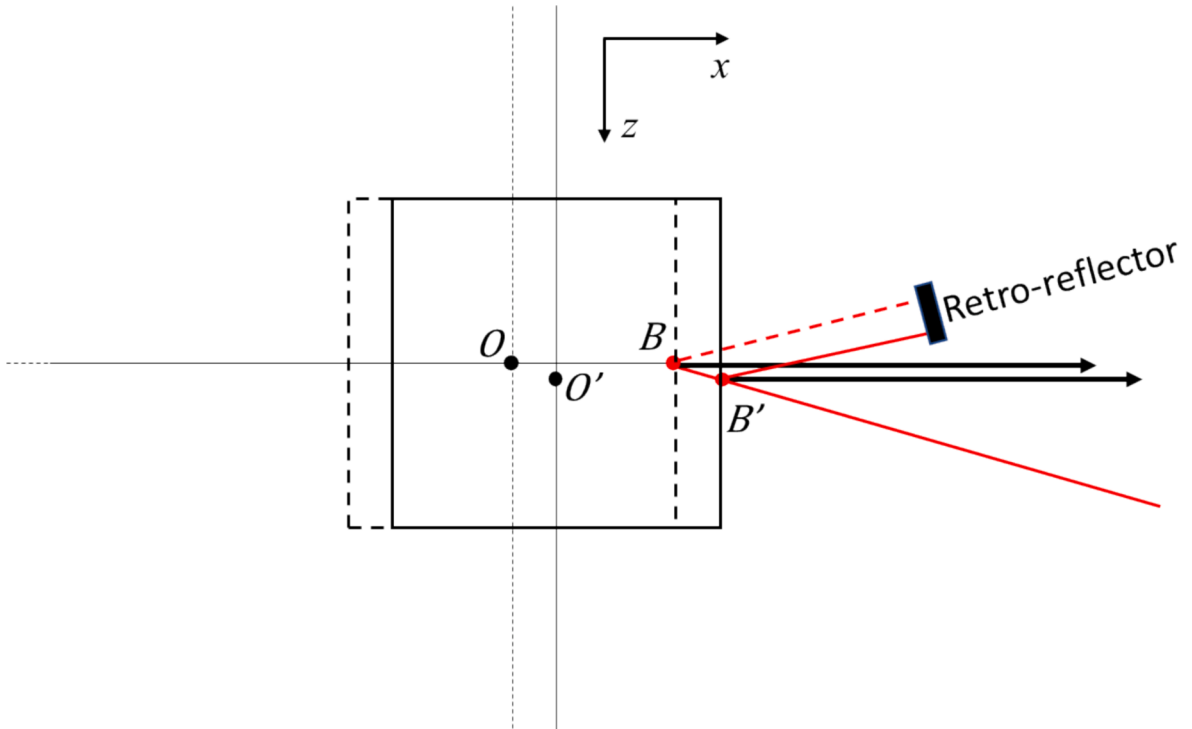


Fig. 8. Change in the axial location of the surface normal unit vector caused by the change in the point of laser beam incidence during x-radial displacement in an x-radial vibration measurement with xz-plane arrangement.

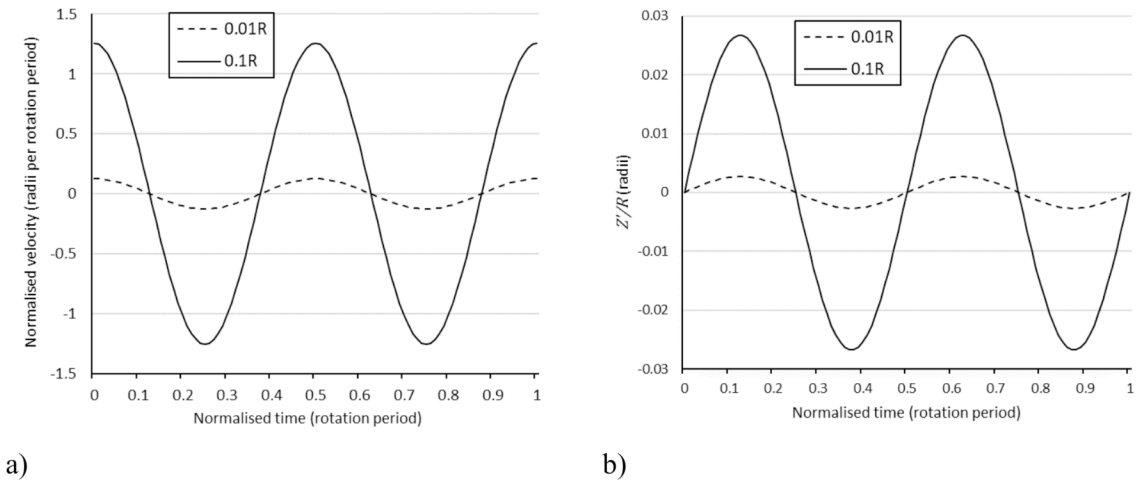


Fig. 9. Simulated x-radial vibration measurement on a rotor with x-radial vibration only and with laser beam incidence in the xz-plane a) Normalised velocity measurement b) Normalised axial shift.

by increasing the ' $\beta b_{1z}$ ' and ' $\beta V_{Oz}$ ' errors, though this will be application specific.

### 3.2.3. Cross-sensitivity to y-radial vibration in a configuration for x-radial vibration measurement

Low cross-sensitivity to y-radial vibration in a configuration for x-radial vibration measurement (and vice-versa) is critically important if this new approach is to be viable. Calculations are presented in this sub-section for the same two laser beam orientations as in the previous sub-section – either the xy-configuration (maximum error in measurement of x-radial vibration) or the xz-configuration (zero error in measurement of x-radial vibration).

For the xy-configuration, Equation (25c) confirms that the axial shift  $Z'$  is zero, because  $b_{1z} = 0$ , while solution of equations

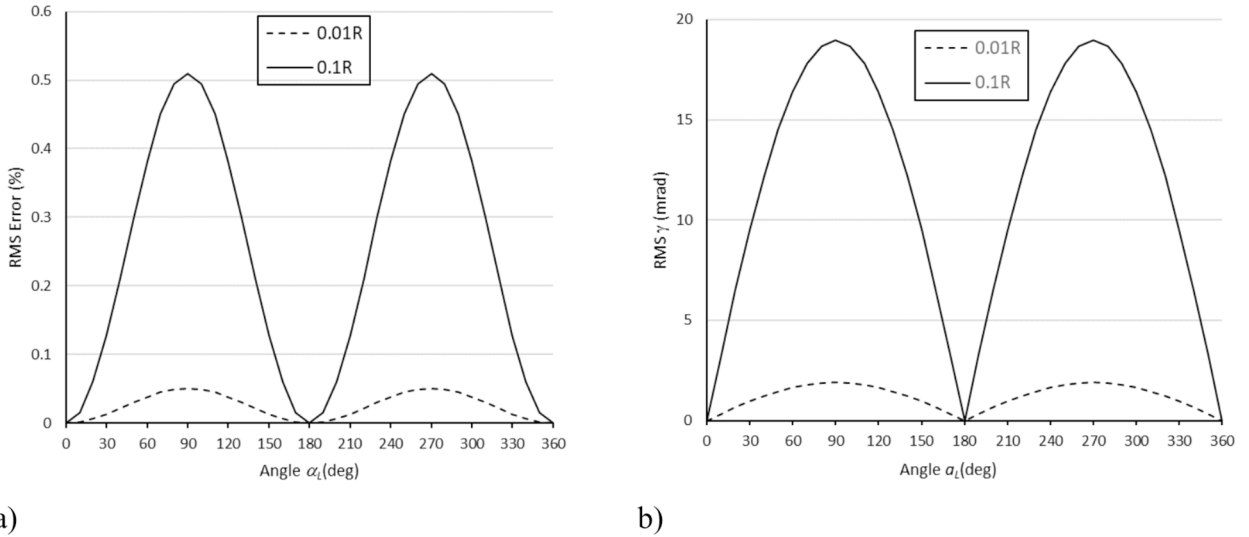


**Fig. 10.** Simulated x-radial vibration measurement on a rotor with x-vibration only: Effect of incident beam orientation a) RMS of the instantaneous error (%) b) RMS  $\gamma$

(25a&b), with  $(\overline{OO^*})_x = 0$ , gives, for example,  $\gamma = -10$  mrad for  $(\overline{OO^*})_y = 0.01R$ . For the  $xz$ -configuration, in which  $b_{1y} = 0$ , solution of equations (25a-c) shows that  $Z$  is small but not zero and, for example,  $\gamma = -10$  mrad for displacement of  $(\overline{OO^*})_y = 0.01R$ . This implies that the cross-sensitivities for the  $xz$  and  $xy$  configurations are practically identical.

Fig. 11a shows a cycle of instantaneous cross-sensitivity for simulated sinusoidal y-displacements with amplitudes 0.01R and 0.1R and frequency equal to rotation frequency. These data are for laser beam incidence in the  $xz$ -plane but they are near-identical to the plots for laser beam incidence in the  $xy$ -plane. The variation of  $\gamma$  through the vibration cycle is shown in Fig. 11b. The plot of  $\gamma$  continues to confirm the validity of the small angle assumption for  $\gamma$ , even at an extreme displacement of 0.1R. Furthermore, combination of equations (21) and (23) shows that the relationship between instantaneous cross-sensitivity and  $\gamma$  is simply:

$$ICS = \frac{-2\gamma b_{1x} V_{Oy}}{-2b_{1x} V_{Oy}} = \gamma \tag{26}$$

Consequently, an instantaneous cross-sensitivity of 1 % is expected at a displacement of  $(\overline{OO^*})_y = 0.01R$ , increasing proportionately to reach 10 % at the extreme amplitude of 0.1R. As for instantaneous error, this cross-sensitivity calculation is a little more pessimistic than one based on the magnitude of spectral peaks. A Magnitude Cross-sensitivity will be calculated based on the ratio

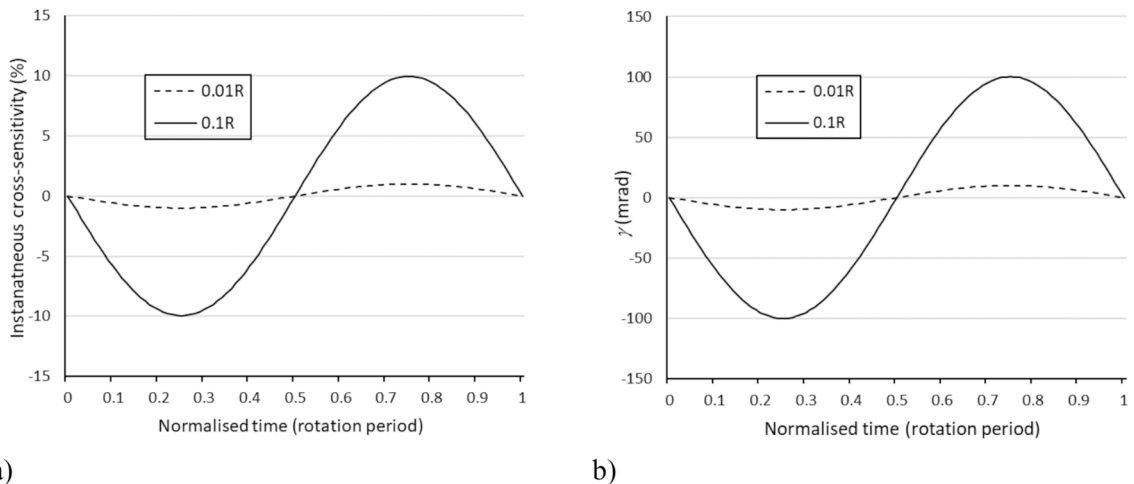


**Fig. 11.** Simulated x-radial vibration measurement on a rotor with y-radial vibration only and with laser beam incidence in the  $xz$ -plane a) Instantaneous cross-sensitivity b) Angle  $\gamma$

between the magnitude from the numerical analysis, at the frequency of interest, and the known simulated magnitude. Before considering this further, however, a more significant matter is that the cross-sensitivity appears primarily at double the frequency of the actual vibration, as shown in Fig. 12a. This occurs as result of dependence on the product between  $\gamma$  and  $V_{Oy}$  seen readily in equation (23).

The corresponding Magnitude Cross-sensitivity (i.e. vibration magnitude apparent at double the actual vibration frequency as a ratio to the simulated vibration magnitude) is shown in Fig. 12b, indicating a linear relationship with the y-radial vibration amplitude. A 5 % Magnitude Cross-sensitivity at the extreme vibration displacement amplitude is considered an acceptable level and confirms that the proposed approach is practically viable. To complete this treatment of cross-sensitivity, Fig. 12c shows the Magnitude Cross-sensitivity at the actual vibration frequency. It is very small but it is matched by an equal magnitude component at three times the vibration frequency (not shown for brevity). These components occur because of the harmonic distortion in  $\gamma$ , specifically they are from the product of  $V_{Oy}$  and the small component of  $\gamma$  at twice vibration frequency.

3.3. Summary of expected errors and cross-sensitivities

Table 1 summarises expected Magnitude Error and Magnitude Cross-sensitivity associated with the two measurement configurations considered, in the presence of x-radial, y-radial, yaw vibrations and certain combinations. These are all calculated by numerical

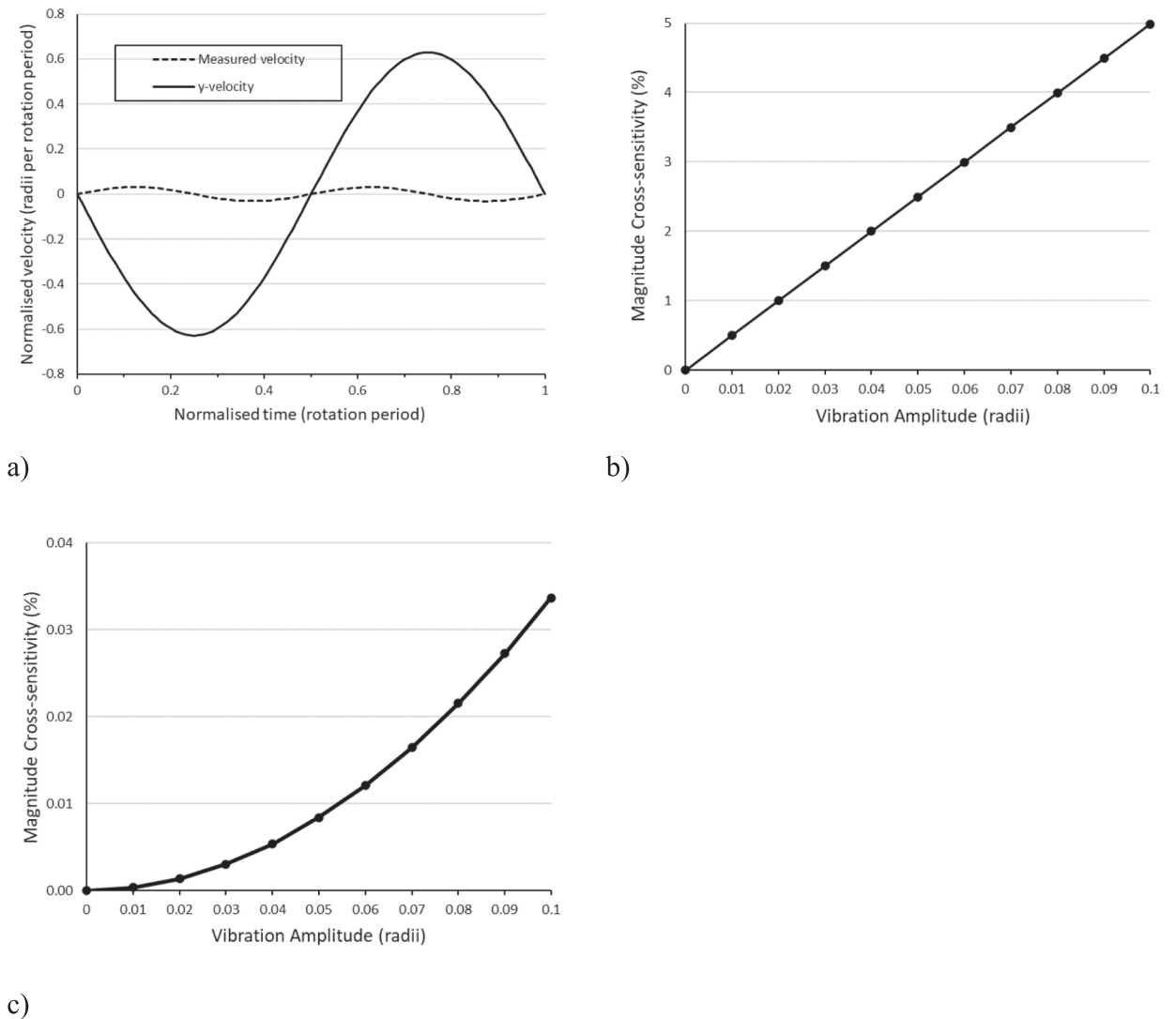


Fig. 12. Simulated x-radial vibration measurement on a rotor with y-radial vibration only and with laser beam incidence in the xz-plane a) Actual y-velocity and measured velocity b) Magnitude Cross-sensitivity at double the actual vibration frequency c) Magnitude Cross-sensitivity based on spectral velocity at the actual vibration frequency.



simulation, for the larger of the vibration displacements considered in the previous sub-sections and, as such, indicate a pessimistic level of error. Row 1 shows the baseline measurement of x-radial vibration in the xy configuration, with very low Magnitude Error and Magnitude Cross-sensitivity. Row 2 shows how all of these low values are reduced to zero when the measurement is made in the xz configuration. In Rows 3 and 4, the addition of a simultaneous yaw vibration is seen to be negligible for the xy configuration but a small increase from zero in the 2x Magnitude Cross-sensitivity appears for the xz configuration. Rows 5 and 6 show how a y-radial vibration causes a near 5 % Magnitude Cross-sensitivity at second order in an x-radial measurement with either configuration, together with very small Magnitude Cross-sensitivities at first and third orders with the xy measurement configuration. Finally, Rows 7 and 8 show how the combination of x-radial and y-radial vibrations causes an elevation in the Magnitude Error, though it is still less than 1 %, and modest increases in the Magnitude Cross-sensitivities.

Overall, these data show that the proposed approach is viable with low errors even in the presence of complex motions with high amplitudes. The xz configuration sees the smallest errors and cross-sensitivities from a theoretical standpoint but the differences are marginal and, as will be shown, these differences are secondary to routine experimental errors. Yaw vibration has very little effect on error while the radial vibration orthogonal to the intended radial measurement gives the greatest error, appearing primarily at twice the actual vibration frequency. Numerical simulations undertaken did not suggest any tendency for multiple vibration components to compound errors in a manner that would render the approach unviable.

#### 4. Experimental validation

##### 4.1. Experimental setups

Fig. 13a&b show the first experimental set-ups used. A rotor is mounted in a cradle which is fixed to a slider rail so that it can oscillate when excited by a shaker through a pushrod, with motion in the x-direction. The rotor is a chrome-plated cylinder of radius 9.4 mm and surface roughness, Ra, 50–80 nm, driven through a flexible belt. In Fig. 13a, the test LDV laser beam path is in the xy-plane, while in Fig. 13b the test LDV laser beam path is in the xz-plane. Both figures show a check LDV and Fig. 13b also shows the location of an accelerometer as another check measurement.

The ‘test’ LDV (Polytec RLV-500 operating in single beam mode) is configured to measure x-radial vibration using the proposed approach. The incident beam is reflected off the rotor and towards a screen, approximately 50 mm from the rotor surface. The screen is coated in a retro-reflective tape (Scotchlite high-gain sheeting type 7610), such that the beam passes back along its original path, first to the point of incidence on the rotor surface and from there back to the LDV collecting optics. A ‘check’ LDV (Polytec OFV-400 operating in single beam mode) is also configured to measure x-vibration but in the traditional normal incidence configuration, with its beam incident at the same point as the ‘test’ LDV and aligned in the x-direction such that it is reflected directly back to the LDV collecting optics. In the earlier tests, an accelerometer mounted on the cradle provided the check measurement (output integrated to give velocity), though its different location makes it a less good comparator and it was superseded in later tests by the check LDV. Measured data were collected by a data acquisition unit sampling at 10 kHz with anti-aliasing filters at 3.9 kHz. Data were typically recorded for 60 s and averaged velocity spectra were then formed from 0.3 s datalengths. As velocity sensitivity is a function of the laser beam angle of incidence, according to equation (7), the appropriate velocity sensitivity value must be input to the settings of the data acquisition unit. For brevity, these velocity spectra are not shown but all analysis is based on spectral magnitudes, presented either in the form of a ratio between check and test measurements, expected value of 1, or alternatively as a Magnitude Difference expressed in the same form as the Magnitude Error in section 3.

Articulation as a *difference* rather than *error* is deliberate as the check measurements can only be estimates of the true vibration velocity based on a more established approach to measurement. Neither the check accelerometer nor the check LDV is an absolute measurement of the true vibration velocity and differences will be associated with contributions from check and test measurements. Differences are readily attributable to two main sources. Firstly, in any back-to-back measurements, small deviations from the nominal instrument calibrations are encountered that can easily result in differences of up to 1 %. Secondly, accurate angular alignment is difficult and a deviation of 1° from the intended orientation in the test LDV setup would result in a 0.5 % error at 15° and 0.8 % error at 25°, according to equation (7). In the case of the accelerometer, the difference is compounded by a different measurement location. Such levels are much greater than the geometrically driven errors in Table 1, which are negligible in this context, with the exception of

**Table 1**  
Typical Magnitude Errors and Cross-sensitivities associated with measurement configurations and calculated by numerical simulation.

Row	Config.	Displacement amplitudes			Phase (rad) x to y or β	Magnitude Error	Magnitude Cross-sensitivity to 1x vibration		
		x-	y-	β(mrad)		1x	1x	2x	3x
1	xy	0.1R	0			0.02 %		To x: 0.36 %	To x: 0.02 %
2	xz	0.1R	0			0 %		To x: 0 %	To x: 0 %
3	xy	0.1R		10	π/2	0.02 %		To x: 0.36 %	To x: 0.02 %
4	xz	0.1R		10	π/2	0 %		To x: 0.13 %	To x: 0 %
5	xy	0	0.1R				To y: 0.03 %	To y: 4.99 %	To y: 0.03 %
6	xz	0	0.1R				To y: 0 %	To y: 4.99 %	To y: 0 %
7	xy	0.1R	0.1R		π/2	0.78 %		To y: 5.35 %	To y: 0.28 %
8	xz	0.1R	0.1R		π/2	0.75 %		To y: 4.99 %	To y: 0.25 %

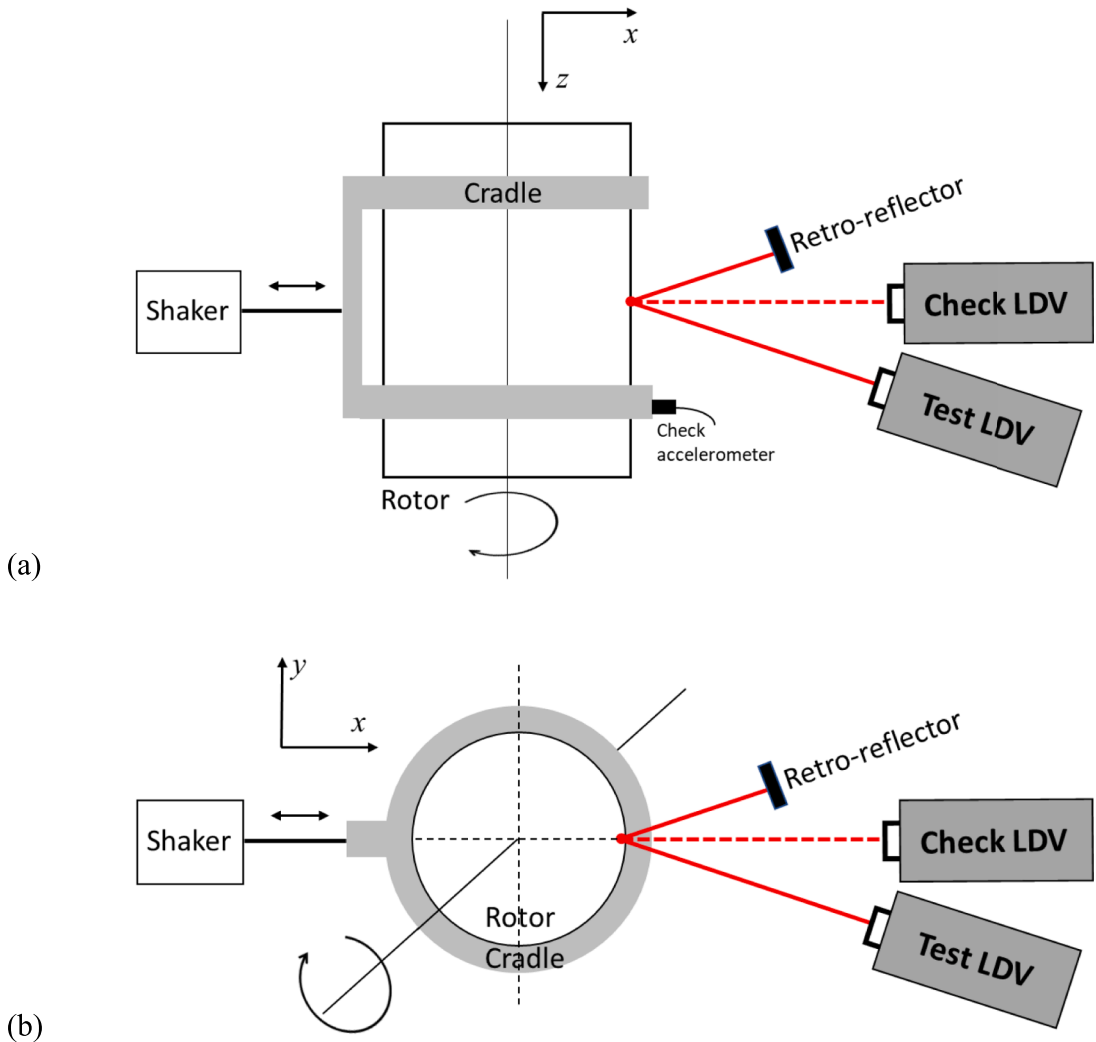


Fig. 13. Experimental set-ups for validation with test LDV laser beam path in the (a)  $xy$ -plane (b)  $xz$  plane.

the second order cross-sensitivity to  $y$ -radial vibration in an  $x$ -radial vibration measurement (rows 5–8).

4.2. Validation of sensitivity to target velocity

The first tests were conducted with broadband excitation (nominally 10 mm/s RMS), comparing the test LDV ( $xz$  configuration) to the accelerometer, in the arrangement shown in Fig. 13b. Ratios between the spectral magnitudes from each velocity measurement are plotted in Fig. 14 as a function of frequency. A ratio of 1, or close to it allowing for experimental error, would confirm the increased sensitivity of the proposed approach, compared to the normal incidence approach, as indicated by equation (4). While the noise from integration of the accelerometer measurement makes the ratio meaningless below 10 Hz, the average ratios from 10-100 Hz are close to 1, at 0.95, 0.96 and 0.98 for 15°, 20° and 25° incidence angles, respectively. An alternative quantification is to calculate an RMS Difference across the full spectral range based on the Magnitude Differences at each spectral line. Values close to zero are expected and those calculated are sufficiently small, at 5.4 %, 4.4 % and 3.0 % for 15°, 20° and 25° incidence angles, respectively, to confirm further the theoretical basis presented for the proposed approach, according to equations (4) and (7), which includes the increased sensitivity of this oblique incidence approach.

Overall, however, the differences are a little larger than might be expected based on consideration of calibration differences and accuracy of alignment. It is also apparent that the ratios are all lower than one, which may be attributed to the different measurement locations (approximately 20 mm apart), particularly that the accelerometer is mounted on a relatively stiff cradle and the laser is incident on a rotor that has a little more freedom to move within its bearings. For this reason, a second LDV was added as a better check device that would allow measurements at the same location on the rotating target. The intention is to make an even more robust assessment of the sensitivity and accuracy of the proposed approach.

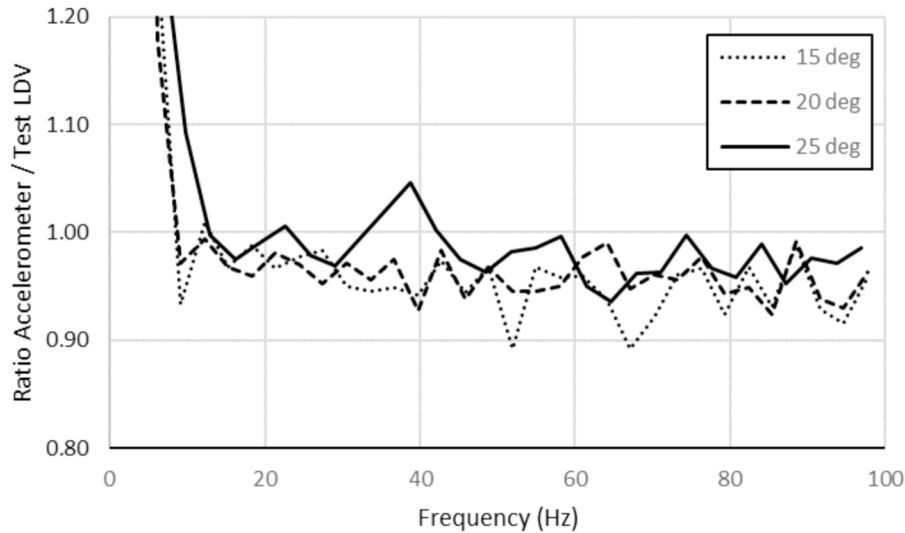


Fig. 14. Ratio between check accelerometer and test LDV spectral magnitudes for broadband excitation at different angles of incidence ( $xz$  configuration, 10 mm/s RMS).

In the next tests presented, the shaker was driven at single frequencies chosen to match (approximately) a desired order of shaft speed. Data such as those shown in Fig. 15 are typical from the measurements taken. The close agreement apparent visually provides a rudimentary confirmation of equation (7). The plots also show elevated noise for the proposed approach, compared to the check LDV, likely to be a consequence of scattering of the laser beam from the retroreflective tape such that the light arriving at the rotor in the return path has the form of a speckle pattern rather than the intensity profile of the original laser beam. Further work should investigate the use of a *retro*-reflector in place of *retro*-reflective tape.

Tests were conducted in  $xy$  and  $xz$  configurations, with single frequency vibrations at rotation orders from 0.5 to 2.5 and at angles of laser beam incidence from  $15^\circ$  to  $25^\circ$ . As shown in Table 2, the Magnitude Differences for these wide-ranging tests are all small. The RMS values for the setups range between 0.98 % and 1.6 %, with the exception of the larger difference at 2nd order and  $25^\circ$ , which the authors believe to be an experimental anomaly. Excluding the anomalous value, the RMS difference at  $25^\circ$  is only 0.59 % (column headed RMS\*). These differences are all consistent with expectations based on calibration differences and alignment accuracy and these data provide an excellent validation of the theoretical basis presented for the proposed approach, according to equation (7).

Experimental noise is also a contributor to the differences; this has been quantified extensively for the check measurement in previous work [7] and is visible also in Fig. 15. The bottom row of Table 2 shows the RMS values at each order with a general trend for the values to increase with increasing order. In these experiments, vibration velocity also tended to reduce with increasing order, allowing a greater influence of experimental noise at the higher orders.

Finally, measurements were made with a broadband excitation and both check LDV and accelerometer measurements. As shown in Fig. 16, where a ratio between measurements of 1 is expected, the strongest agreement is found between check LDV and test LDV measurements for the Magnitude Differences which have an RMS of 1.1 % (from 0-100 Hz). This is similar to the values calculated for single frequency vibrations and shown in Table 2. When the ratio is formed between the integrated accelerometer and test LDV measurements, Fig. 16 still shows good agreement but a larger divergence; the RMS of the Magnitude Differences is 2.8 % (from 3-100 Hz), which is comparable with the differences shown in Fig. 14. This supports the proposition that the differences apparent in Fig. 14 were slightly larger than expected because the check accelerometer is a less good comparator.

The experimental results presented in this sub-section have consistently shown Magnitude Differences with RMS values around 1 % between a measurement with the new approach and the best check measurement possible. Differences of this size are readily attributable to small alignment differences and small calibration errors. Such small differences confirm that the proposed approach is robust and accurate, including that the theoretical prediction of higher velocity sensitivity is correct. These data also show that the fundamental geometric errors associated with the approach, which have been explored theoretically, are negligible compared to inevitable errors encountered in real measurements. This means there is no practical difference between  $xy$ - and  $xz$ -configurations or, for that matter, any of the orientations indicated by Fig. 3.

#### 4.3. Validation of cross-sensitivity to radial vibration in the direction orthogonal to the intended measurement

The second set of experiments conducted considered the cross-sensitivity of measurements in one radial direction to motion in the other, described in the theoretical analysis as cross-sensitivity to  $y$ -radial vibration in a configuration for  $x$ -vibration measurement. This cross-sensitivity is the only drawback for the proposed approach but the levels predicted and encountered are low enough for this to be outweighed by the benefits.

The measurements were achieved by realigning the test LDV and redefining the  $x$ - and  $y$ -directions, as shown in Fig. 17. The shaker

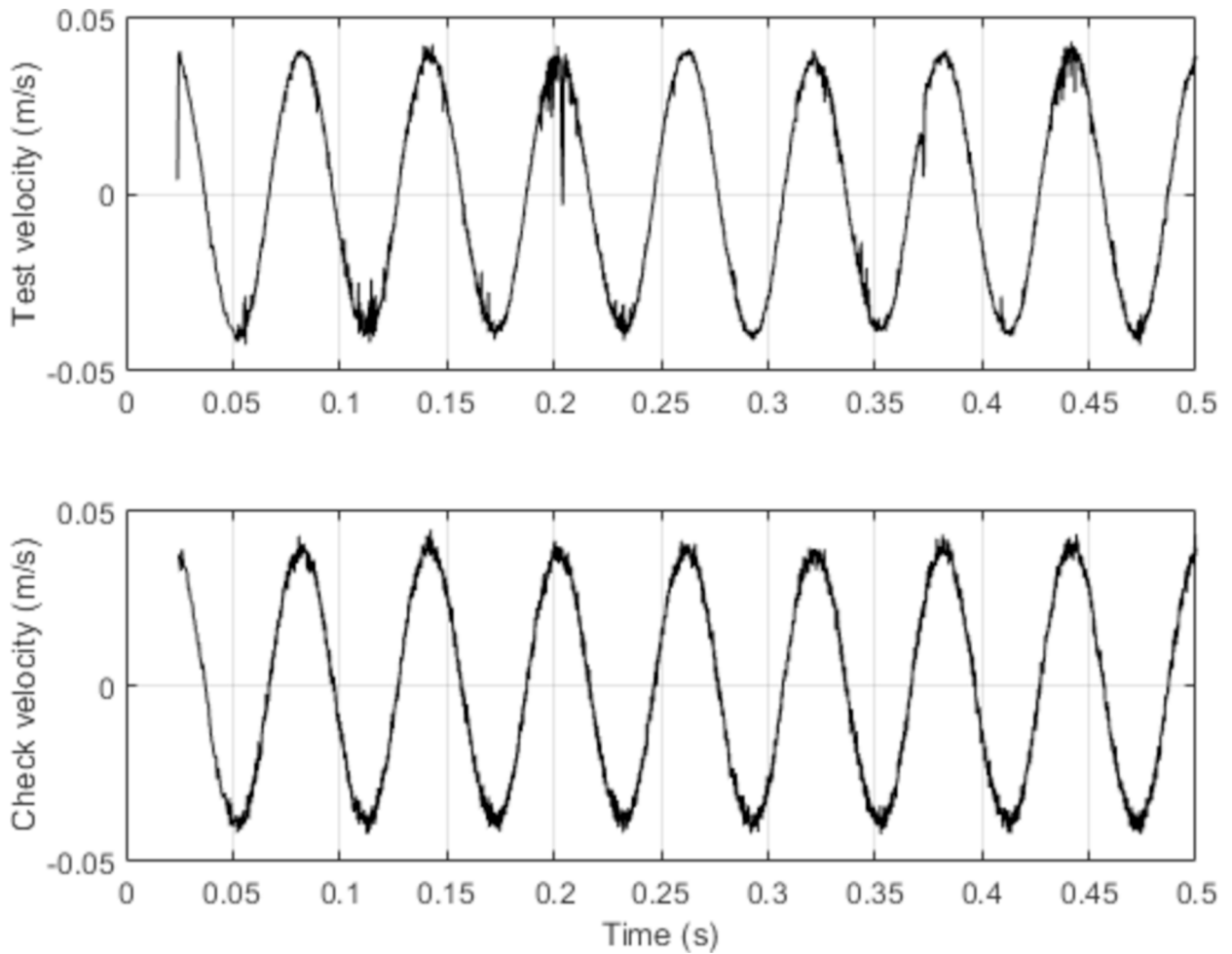


Fig. 15. Typical data from the experimental validation. Upper: time history of single frequency vibration from the test LDV (xy configuration). Lower: time history of single frequency vibration from the check LDV.

Table 2

Magnitude Differences between test and check measurements for excitation at specific vibration orders, in xy and xz configurations and at 3 angles of laser beam incidence.

Angle of incidence (deg)	Config.	Vibration orders					RMS	RMS*
		0.5	1	1.5	2	2.5		
15	xy	0.04 %	0.12 %	1.01 %	1.01 %	1.64 %	0.98 %	
15	xz	1.78 %	1.35 %	1.13 %	1.56 %	2.02 %	1.60 %	
20	xz	-0.32 %	-0.77 %	-1.21 %	-2.01 %	-0.48 %	1.13 %	
25	xz	0.35 %	-0.68 %	-0.49 %	6.33 %	0.76 %	2.88 %	0.59 %
RMS at each order		0.92 %	0.85 %	1.00 %	1.58 %	1.38 %		

sits behind the rotor, in the view given, and causes the rotor, which is mounted on a rail via the cradle, to oscillate in the y-direction.

This motion in the y-radial direction results in a cross-sensitivity peak in the x-radial vibration measurement at twice the excitation frequency, as first described in sub-section 3.2.3. The experimental Magnitude Cross-sensitivities are calculated in the same way as the numerical values in sub-section 3.2.3, i.e. from the spectral peak at excitation frequency in the check LDV measurement (best available estimate of the genuine vibration) and from the spectral peak at twice excitation frequency in the test LDV measurement.

In Fig. 18, the experimental values are marked with crosses and the theoretical (solid) line is the same as in Fig. 12b. As the cross-sensitivity is just a few percent, the associated peaks are relatively small and so significantly affected by noise in the measurement. As a consequence, the agreement between theoretical and experimental Magnitude Cross-sensitivities is generally better at the lower frequencies (half and first order) where displacement amplitudes were higher, but generally less good where displacements were lower (particularly at Orders 1.5 and 2), as shown in Table 3. Nonetheless, the agreement overall is strong, as confirmed in both Fig. 18 and

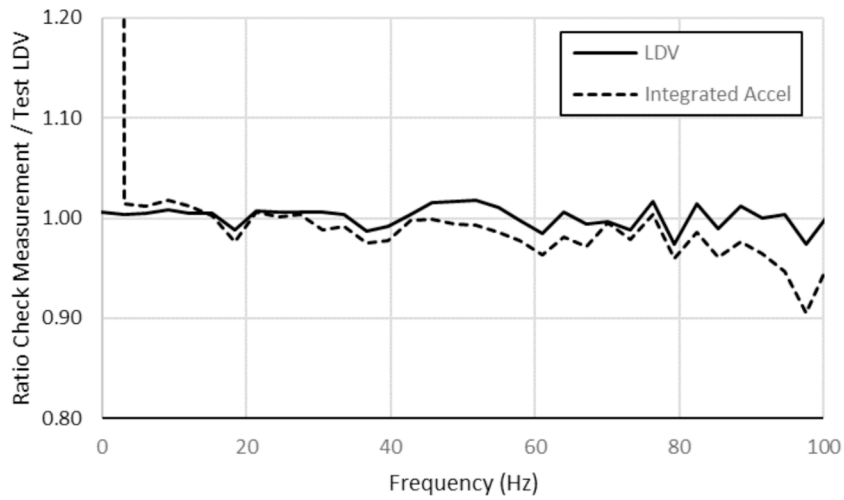


Fig. 16. Ratios between check measurements and test LDV spectral magnitudes for broadband excitation (xy configuration 20 mm/s RMS).

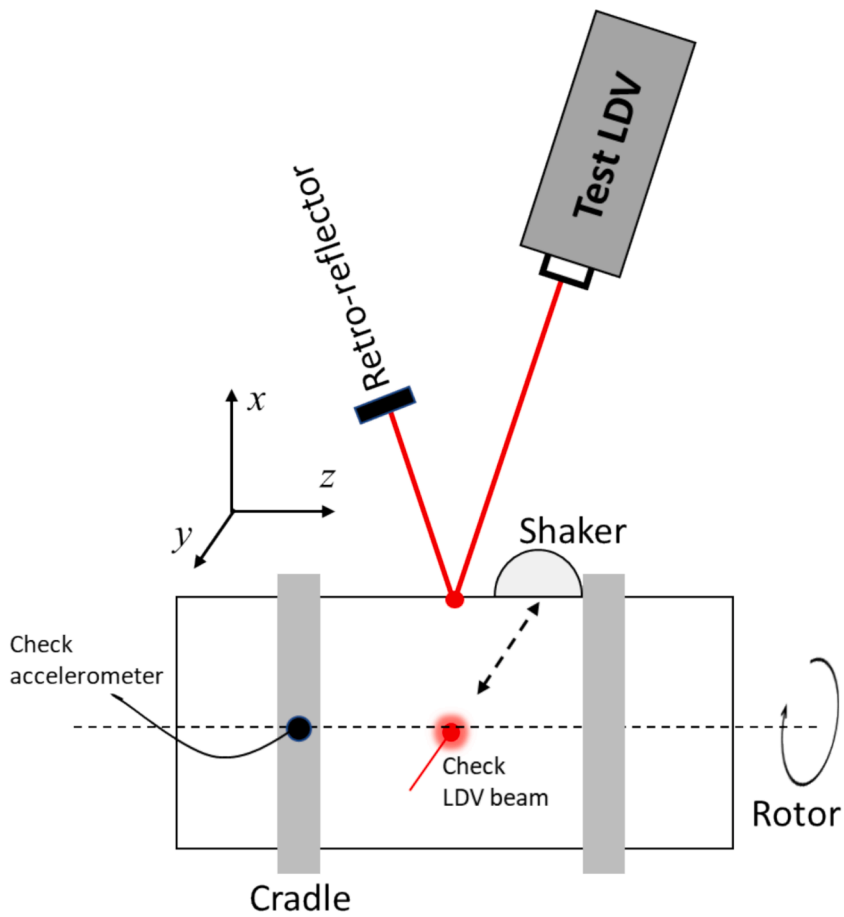


Fig. 17. Experimental validation of the cross-sensitivity apparent for the proposed approach.

Table 3, further validating the theoretical basis of the proposed approach, according to equation (7).

For the specific measurements made here, cross-sensitivity levels can be compared to those that would be encountered in the two alternative measurement approaches, i.e. with normal incidence on either a polished-circular rotor or a rough rotor (which would require covering the rotor surface with retroreflective tape). For the polished circular rotor with normal incidence, the cross-sensitivity

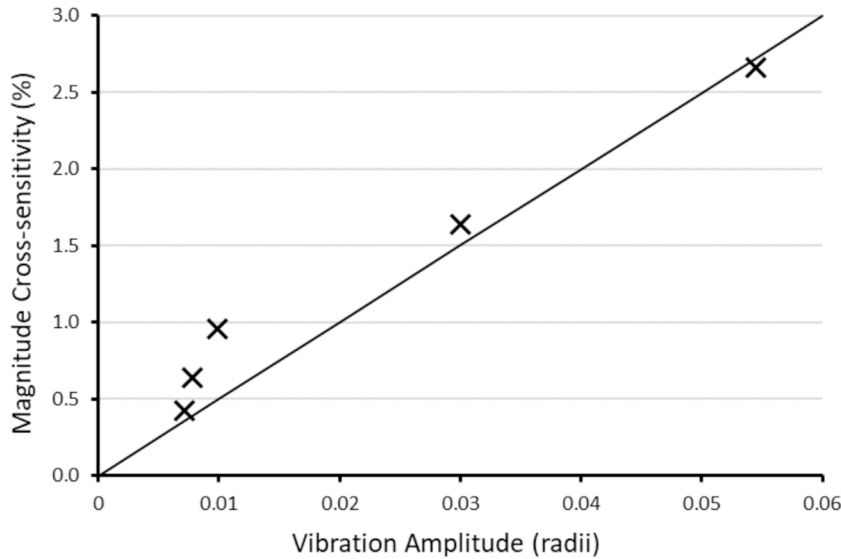


Fig. 18. Experimental validation of the Magnitude Cross-sensitivity to y-vibration in an x-vibration measurement (xz configuration) for the proposed approach.

Table 3

Experimental validation of the Magnitude Cross-sensitivity to y-radial vibration in an x-radial vibration measurement (xz-configuration) for the proposed approach.

Vibration order	0.5	1	1.5	2	2.5
Displacement (radii)	0.054	0.030	0.0098	0.0078	0.0071
Experimental cross-sensitivity	2.66 %	1.64 %	0.96 %	0.64 %	0.43 %
Theoretical cross-sensitivity	2.72 %	1.50 %	0.49 %	0.39 %	0.36 %

levels can only be obtained empirically [7]. The closest data available are for laser beam diameters of 90 mm and 520 mm (the RLV-500 optical head used here had a beam diameter of approximately 190 μm) and rotors with surface roughness of 44 nm and 100 nm. (the rotor used here had surface roughness of 50–80 nm). Consequently, the low end of the likely cross-sensitivity range is estimated by the combination of 90 μm laser beam and 50 nm surface roughness and the upper range by the combination of 520 μm laser beam and 100 nm surface roughness, as shown in Table 4. The values are shown rounded down to the nearest 5 %. In the case of the displacement values of 270 % and 150 % beam diameter for the 520 μm laser beam, cross-sensitivity has been estimated based on the nearest available data point (approximately 85 % cross sensitivity for vibration displacement of 120 % beam diameter) and trajectory at that point.

For the equivalent measurement on a rough rotor, the cross-sensitivity is simply given by the ratio of rotation frequency to vibration frequency [7], as shown in Table 5. The cross-sensitivity values are very high but it is well established that a resolution procedure must be followed for the rough rotor measurements. Comparing cross-sensitivities directly might, therefore, be regarded as an unfairly harsh comparison. For this reason, Table 5 also shows the likely error in a resolved measurement [7]. While this is no longer a direct comparison, it provides a better indication of the consequences of y-radial vibration in an x-radial vibration measurement. Note how the first order component cannot be resolved for the rough rotor measurement. For the other orders, the proposed approach proves a good match at the 0.5 order and a better option thereafter.

Notwithstanding the complication that the cross-sensitivity occurs mainly at twice the actual vibration frequency, it is clear from Tables 4 and 5 that the levels encountered for the proposed approach are generally lower and sometimes much lower than those associated with the existing approaches.

### 5. Further work

There are three priorities for further work and they are presented here in order of importance. The first is to explore performance for varying levels of surface roughness. These experiments used a rotor with roughness between 50–80 nm so more polished rotors will give reliable results but performance of rotors with roughness above 80 nm requires further experimentation to identify the upper limit of surface roughness at which the approach can be deployed. This can be combined with investigation of the effect of roundness, which might be primarily numerical because obtaining test rotors with controlled out-of-roundness is difficult. Out-of-roundness for the rotor used in these experiments was measured at 30 μm (maximum deviation from nominal circle). Out-of-roundness is not expected to be problematic because typical levels will just result in small deviations in the direction of the surface normal but it would be valuable to

**Table 4**

Comparison between Magnitude Cross-sensitivity to *y*-radial vibration in an *x*-radial vibration measurement (*xz*-configuration) for the proposed approach and the normal incidence approach.

Vibration order	0.5	1	1.5	2	2.5
Displacement (radii)	0.054	0.030	0.0098	0.0078	0.0071
Displacement as % beam diameter (190 μm)	270 %	150 %	50 %	40 %	35 %
Normal incidence approach: estimate of low-end cross sensitivity (90 μm beam, 44 nm roughness)	95 %	70 %	5 %	5 %	5 %
Normal incidence approach: estimate of high-end cross sensitivity (520 μm beam, 100 nm roughness)	>90 %	>90 %	20 %	15 %	10 %
Proposed approach: theoretical cross-sensitivity	2.72 %	1.50 %	0.49 %	0.39 %	0.36 %

**Table 5**

Comparison between Magnitude Cross-sensitivity to *y*-vibration in an *x*-vibration measurement (*xz*-configuration) for the proposed approach and the rough rotor approach.

Vibration order	0.5	1	1.5	2	2.5
Displacement (radii)	0.054	0.030	0.0098	0.0078	0.0071
Rough rotor cross sensitivity	200 %	100 %	67 %	50 %	40 %
Proposed approach theoretical cross-sensitivity	2.72 %	1.50 %	0.49 %	0.39 %	0.36 %
Rough rotor typical error after resolution [7]	2-3 %	N/A	2-3 %	1-2 %	0.5-1 %

confirm and quantify this. The second is to incorporate a retroreflector cube into the optical configuration as an alternative to the *retro*-reflective tape used in the experiments reported in this paper. The aim will be to reduce the higher level of noise apparent in Fig. 15 for the new approach.

Finally, a numerical investigation of the errors associated with inevitable misalignments will give further confidence in the new approach. An initial analysis has been made, for the *xz* configuration, in which  $\beta_L$  has an intended value of  $15^\circ$  and misalignments with standard deviation of  $0.25^\circ$ , translational misalignments,  $\Delta y_A$ , have a mean of zero and a standard deviation of 0.0333R (0.3 mm on a rotor of radius 9.4 mm, as used in these experiments) and angular misalignments around the *z*-axis,  $\rho$ , have a mean of zero and a standard deviation of 11 mrad. The misalignment values were chosen based on practical experience from experiments and each variable has a normal distribution. The translational misalignment appears in equation (14b) while the angular misalignments can be incorporated into a modified equation (15) as:

$$\hat{b}_1 = [\hat{x} \ \hat{y} \ \hat{z}] [y, \theta] [-\cos \rho \ \sin \rho \ 0]^T \tag{26}$$

One hundred thousand alignment scenarios were generated and the results are shown in Fig. 19, which indicates that the associated error is predicted to be less than 0.5 % for 97 % of the time. This magnitude of error is consistent with experimental results obtained and appropriate for a viable measurement approach.

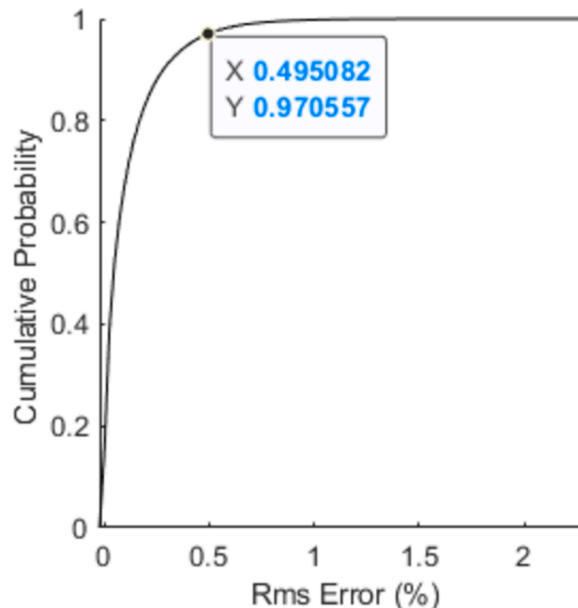


**Fig. 19.** Cumulative Probability for RMS error associated with inevitable misalignments.



## 6. Conclusions

A new laser vibrometry approach for radial vibration measurement directly from a polished-circular rotor has been proposed. The approach uses oblique incidence and the inclusion of a *retro*-reflecting surface to overcome limitations associated with the standard normal incidence configuration for such a measurement. Operation has been modelled theoretically and performance has been explored numerically and validated experimentally, with excellent agreement shown. Low measurement error, in the region of 1 %, has been found, alongside an amplitude-dependent cross-sensitivity to the orthogonal radial vibration component of up to 2–3 % for typical vibration amplitudes. This cross-sensitivity, which appears at twice the frequency of the associated vibration, is the most significant limitation identified for the approach but it is much less problematic than the effects of the same orthogonal vibration in equivalent measurements on rough or polished rotors with normal incidence. For these reasons, the authors now recommend this new approach as the most reliable method for radial vibration measurements directly from a rotor using laser vibrometry.

### CRedit authorship contribution statement

**Ben Gunn:** Writing – original draft, Validation, Software, Methodology, Investigation, Formal analysis, Data curation. **Steve Rothberg:** Writing – review & editing, Writing – original draft, Validation, Supervision, Resources, Project administration, Methodology, Investigation, Formal analysis, Data curation, Conceptualization.

### Declaration of competing interest

The authors declare that they have no known competing financial interests or personal relationships that could have appeared to influence the work reported in this paper.

### Acknowledgement

The authors acknowledge the support of the Wolfson School of Mechanical, Electrical and Manufacturing Engineering at Loughborough University where they were both based when the first stages of the theoretical work and all of the experimental work were conducted.

### Appendix A.: Rotation matrices

In the vector approach presented in this paper, rotation matrices are a convenient means to introduce important features such as laser beam orientation and angular misalignment, and variations in the direction of the shaft rotation axis. The matrices are dependent on the axis around which the rotation is performed. For rotations  $\alpha$ ,  $\beta$  and  $\gamma$  around, respectively, the  $x$ -,  $y$ - and  $z$ -axes, the appropriate rotation matrices are as follows [22]:

$$[x, \alpha] = \begin{bmatrix} 1 & 0 & 0 \\ 0 & \cos\alpha & -\sin\alpha \\ 0 & \sin\alpha & \cos\alpha \end{bmatrix} \quad (\text{A1a})$$

$$[y, \beta] = \begin{bmatrix} \cos\beta & 0 & \sin\beta \\ 0 & 1 & 0 \\ -\sin\beta & 0 & \cos\beta \end{bmatrix} \quad (\text{A1b})$$

$$[z, \gamma] = \begin{bmatrix} \cos\gamma & -\sin\gamma & 0 \\ \sin\gamma & \cos\gamma & 0 \\ 0 & 0 & 1 \end{bmatrix} \quad (\text{A1c})$$

The matrices can be applied singly or in series. Where rotations around more than one axis are by large angles (e.g. for laser beam orientation), their order must be maintained. When rotations are by small angles (e.g. for angular vibrations and misalignments), this is not necessary.

### Appendix B.: Expanding LHS of equation (16)

The LHS of equation (16) is:  $Z \hat{z}_R + [\hat{x}_R \hat{y}_R \hat{z}_R][z, \gamma][R \ 0 \ 0]^T$

Substituting equation (A1c) into the second term of the LHS of equation (16) and expanding gives:

$$[\hat{x}_R \hat{y}_R \hat{z}_R] \begin{bmatrix} \cos\gamma & -\sin\gamma & 0 \\ \sin\gamma & \cos\gamma & 0 \\ 0 & 0 & 1 \end{bmatrix} \begin{bmatrix} R \\ 0 \\ 0 \end{bmatrix} = [\hat{x}_R \hat{y}_R \hat{z}_R] \begin{bmatrix} R\cos\gamma \\ R\sin\gamma \\ 0 \end{bmatrix} \quad (\text{B1a})$$

The full LHS of equation (16) can then be rewritten as:

$$Z' \begin{bmatrix} \hat{x}_R \\ \hat{y}_R \\ \hat{z}_R \end{bmatrix} + [\hat{x}_R \ \hat{y}_R \ \hat{z}_R][z, \gamma] \begin{bmatrix} R \\ 0 \\ 0 \end{bmatrix} = [\hat{x}_R \ \hat{y}_R \ \hat{z}_R] \begin{bmatrix} R \cos \gamma \\ R \sin \gamma \\ Z' \end{bmatrix} \quad (\text{B1b})$$

The coordinate transformation, see equation (9), using the rotation matrices, equations (A1a) and (A1b), can be expanded as:

$$[\hat{x}_R \ \hat{y}_R \ \hat{z}_R] = [\hat{x} \ \hat{y} \ \hat{z}] \begin{bmatrix} \cos \beta & 0 & \sin \beta \\ \sin \alpha \sin \beta & \cos \alpha & -\sin \alpha \cos \beta \\ -\cos \alpha \sin \beta & \sin \alpha & \cos \alpha \cos \beta \end{bmatrix} \quad (\text{B2})$$

Substituting equation (B2) into the RHS of equation (B1b) and completing the matrix multiplication allows the LHS of equation (16) to be written in terms of the global coordinates as:

$$[\hat{x}_R \ \hat{y}_R \ \hat{z}_R] \begin{bmatrix} R \cos \gamma \\ R \sin \gamma \\ Z' \end{bmatrix} = [\hat{x} \ \hat{y} \ \hat{z}] \begin{bmatrix} R \cos \gamma \cos \beta + Z' \sin \beta \\ R \cos \gamma \sin \alpha \sin \beta + R \sin \gamma \cos \alpha - Z' \sin \alpha \cos \beta \\ -R \cos \gamma \cos \alpha \sin \beta + R \sin \gamma \sin \alpha + Z' \cos \alpha \cos \beta \end{bmatrix} \quad (\text{B3})$$

### Appendix C.: Investigating scenarios based on equations (25a-c)

A manageable solution of equations (25a-c) begins by substituting equation (25c) into equations (25a&b) and then neglecting double angles. This gives:

$$\cos \gamma \approx (b_{1x} - \beta b_{1z}) \left( \frac{p}{R} \right) + \left( 1 - \beta \frac{\Delta z_A}{R} - \frac{(\overline{OO^*})_x}{R} + \beta \frac{(\overline{OO^*})_z}{R} \right) \quad (\text{C1a})$$

$$\sin \gamma \approx (b_{1y} + a b_{1z}) \left( \frac{p}{R} \right) + \left( \frac{\Delta y_A}{R} + \alpha \frac{\Delta z_A}{R} - \frac{(\overline{OO^*})_y}{R} - \alpha \frac{(\overline{OO^*})_z}{R} \right) \quad (\text{C1b})$$

Squaring equations (C1a&b) and adding gives a quadratic equation in  $\left( \frac{p}{R} \right)$  of the form:

$$a_1 \left( \frac{p}{R} \right)^2 + a_2 \left( \frac{p}{R} \right) + a_3 = 0 \quad (\text{C2a})$$

in which:

$$a_1 = (b_{1x} - \beta b_{1z})^2 + (b_{1y} + a b_{1z})^2 \quad (\text{C2b})$$

$$a_2 = 2(b_{1x} - \beta b_{1z}) \left( 1 - \beta \frac{\Delta z_A}{R} - \frac{(\overline{OO^*})_x}{R} + \beta \frac{(\overline{OO^*})_z}{R} \right) + 2(b_{1y} + a b_{1z}) \left( \frac{\Delta y_A}{R} + \alpha \frac{\Delta z_A}{R} - \frac{(\overline{OO^*})_y}{R} - \alpha \frac{(\overline{OO^*})_z}{R} \right) \quad (\text{C2c})$$

$$a_3 = \left( 1 - \beta \frac{\Delta z_A}{R} - \frac{(\overline{OO^*})_x}{R} + \beta \frac{(\overline{OO^*})_z}{R} \right)^2 + \left( \frac{\Delta y_A}{R} + \alpha \frac{\Delta z_A}{R} - \frac{(\overline{OO^*})_y}{R} - \alpha \frac{(\overline{OO^*})_z}{R} \right)^2 - 1 \quad (\text{C2d})$$

As a quadratic equation, two solutions for  $\left( \frac{p}{R} \right)$  are found. These correspond to the intersections of the laser beam path with the near and the far surfaces of the rotor. As formulated in this paper, the required solution is always the smallest of the absolute values. Taking this and returning to equation (C1a) or (C1b), the angle  $\gamma$  is found. Finally,  $\left( \frac{z}{R} \right)$  is found by substituting back into equation (25c).

In the scenarios for [section 3](#), misalignments and the angular target vibrations are set to zero. This simplifies equations (C2b-d) as follows:

$$a_1 = b_{1x}^2 + b_{1y}^2 \quad (\text{C3a})$$

$$a_2 = 2b_{1x} \left( 1 - \frac{(\overline{OO^*})_x}{R} \right) + 2b_{1y} \left( -\frac{(\overline{OO^*})_y}{R} \right) \quad (\text{C3b})$$

$$a_3 = \left(1 - \frac{(\overline{OO^z})_x}{R}\right)^2 + \left(\frac{(\overline{OO^z})_y}{R}\right)^2 - 1 \tag{C3c}$$

Without angular vibrations, the surface normal, see equation (19b), can also be written more simply as:

$$\hat{n}_B = \cos\gamma \hat{x} + \sin\gamma \hat{y} \tag{C4}$$

To calculate the instantaneous measurement error, equation (C4) is first combined with equation (6) to give:

$$U_m = -2(\cos\gamma b_{1x} + \sin\gamma b_{1y})(\cos\gamma V_{O_x} + \sin\gamma V_{O_y}) \tag{C5}$$

For the first two scenarios (sub-sections 3.2.1 and 3.2.2), in which an x-radial measurement is made in the presence of only x-radial vibration, i.e.  $V_{O_y} = 0$ , an instantaneous error is calculated based on equation (20) and incorporating equation (C5) as:

$$IE = 1 - \cos^2\gamma - \sin\gamma\cos\gamma \frac{b_{1y}}{b_{1x}} \tag{C6}$$

For the second two scenarios (section 3.2.3), in which an x-measurement is made in the presence of only y-radial vibration, i.e.  $V_{O_x} = 0$ , an instantaneous cross-sensitivity is calculated based on equation (21) and incorporating equation (C5) as:

$$ICS = \cos\gamma\sin\gamma + \sin^2\gamma \frac{b_{1y}}{b_{1x}} \tag{C7}$$

The dependence of the coefficients in equation (C2a) on the vibration  $\overline{OO^z}$  makes  $\left(\frac{p}{R}\right)$  time dependent, which in turn makes at least one of  $\gamma$  and  $\frac{z}{R}$  time dependent too. Consequently, equations (25a-c) must be solved for every increment of  $\overline{OO^z}$ . Specific values are shown in the sub-sections of this Appendix for illustrative purposes but they are associated only with the instantaneous  $\overline{OO^z}$  vector.

Scenario 1: x-radial measurement on a rotor with x-radial vibration only, incident laser beam orientation in the xy-plane

In this first scenario,  $b_{1z} = 0$  and  $\left(\overline{OO^z}\right)_y = 0$ . Consequently:

$$a_1 = b_{1x}^2 + b_{1y}^2 = 1 \tag{C8a}$$

$$a_2 = 2b_{1x} \left(1 - \frac{(\overline{OO^z})_x}{R}\right) \tag{C8b}$$

$$a_3 = \left(\frac{(\overline{OO^z})_x}{R}\right)^2 - 2\left(\frac{(\overline{OO^z})_x}{R}\right) \tag{C8c}$$

$\left(\frac{p}{R}\right)$  is then calculated from equation (C2a), allowing  $\gamma$  to be calculated from equation (C1b) as:

$$\gamma = \sin^{-1}\left(\frac{p}{R}\right)b_{1y} \tag{C9}$$

Equation (25c) shows readily that  $\left(\frac{z}{R}\right) = 0$ .

In the main body of the paper,  $\gamma$  and the instantaneous error, from equation (C6), are plotted as a continuous function of normalised time but here, in Table C1, they are calculated, for illustrative purposes, just at instantaneous x-radial displacements of  $\left(\overline{OO^z}\right)_x = \pm 0.1R$ . It is observed that the values of  $\gamma$  at each end of the vibration cycle differ very slightly and that the corresponding errors differ by a greater margin.

**Table C1**  
Instantaneous solutions to equations (25a-c) and calculation of measurement error for scenario 1 (angle of incidence 15°).

$\frac{(\overline{OO^z})_x}{R}$	$\left(\frac{p}{R}\right)$	$\gamma$ (mrad)	$\frac{z}{R}$	Instantaneous error %
0.1	0.1032	-26.7	0	-0.644
-0.1	0.1039	26.9	0	0.793

Scenario 2:  $x$ -radial measurement on a rotor with  $x$ -radial vibration only, incident laser beam orientation in the  $xz$ -plane.

For this scenario,  $b_{1y} = 0$  and  $(\overline{OO^*})_y = 0$ . This leads to quite a simple solution as equation (C1b) shows readily that  $\gamma = 0$ . Equation (C1a) also simplifies to give:

$$\left(\frac{p}{R}\right) = \frac{1}{b_{1x}} \frac{(\overline{OO^*})_x}{R} \tag{C10a}$$

while equation (25c) reduces to:

$$\left(\frac{Z}{R}\right) = \frac{(\overline{OO^*})_x}{R} \frac{b_{1z}}{b_{1x}} \tag{C10b}$$

which shows how  $Z$  scales as  $\frac{b_{1z}}{b_{1x}}$  of the vibration displacement, i.e. to the tan of the incident angle (0.268 for  $15^\circ$  incidence). More importantly, equation (C6) shows that the instantaneous error is zero because  $\gamma = 0$  irrespective of vibration displacement. In the main body of the paper,  $\frac{Z}{R}$  and the instantaneous error are plotted as a continuous function of normalised time but here, in Table C2, they are calculated, for illustrative purposes, just at instantaneous  $x$ -displacements of  $(\overline{OO^*})_x = \pm 0.1R$ .

**Table C2**

Instantaneous solutions to equations (25a-c) and calculation of instantaneous error for scenario 2 (angle of incidence  $15^\circ$ ).

$\frac{(\overline{OO^*})_x}{R}$	$\left(\frac{p}{R}\right)$	$\gamma(\text{mrad})$	$\frac{Z}{R}$	Instantaneous error %
0.1	-0.1035	0	0.0268	0
-0.1	0.1035	0	-0.0268	0

Scenario 3:  $x$ -radial measurement on a rotor with  $y$ -radial vibration only, incident laser beam orientation in the  $xy$  plane.

In this scenario,  $b_{1z} = 0$  and  $(\overline{OO^*})_x = 0$ . Consequently

$$a_1 = b_{1x}^2 + b_{1y}^2 = 1 \tag{C11a}$$

$$a_2 = 2b_{1x} - 2b_{1y} \left( \frac{(\overline{OO^*})_y}{R} \right) \tag{C11b}$$

$$a_3 = \left( \frac{(\overline{OO^*})_y}{R} \right)^2 \tag{C11c}$$

$\left(\frac{p}{R}\right)$  is then calculated from equation (C2a), allowing  $\gamma$  to be calculated from equation (C1b) as:

$$\gamma = \sin^{-1} \left( \left(\frac{p}{R}\right) b_{1y} - \frac{(\overline{OO^*})_y}{R} \right) \tag{C12}$$

Equation (25c) shows readily that  $\left(\frac{Z}{R}\right) = 0$  and the instantaneous cross-sensitivity to  $y$ -radial vibration can then be calculated. In the main body of the paper,  $\gamma$  and the cross-sensitivity, from equation (C7), are considered as a continuous function of normalised time but here, in Table C3, they are shown for illustrative purposes at instantaneous  $y$ -radial displacements of  $(\overline{OO^*})_y = \pm 0.01R$  and  $\pm 0.1R$ . It is observed, from the larger displacement, that the values of  $\gamma$  at each end of the vibration cycle differ very slightly, as do the corresponding cross-sensitivities.

**Table C3**

Instantaneous solutions to equations (25a-c) and calculation of instantaneous cross-sensitivity for scenario 3 (angle of incidence 15°).

$\frac{(\overline{OO^*})_y}{R}$	$\left(\frac{p}{R}\right)$	$\gamma(\text{mrad})$	$\frac{Z}{R}$	Instantaneous Cross-sensitivity %
0.01	0.00005163	-10.0	0	-1.00
-0.01	0.00005190	10.0	0	1.00
0.1	0.005054	-98.9	0	-10.1
-0.1	0.005334	101.6	0	9.81

Scenario 4: x-radial measurement on a rotor with y-radial vibration only, incident laser beam orientation in the xz plane.

In this scenario,  $b_{1y} = 0$  and  $(\overline{OO^*})_x = 0$ . This leads to quite a simple solution as equation (C1b) shows that:

$$\gamma = \sin^{-1} \left( - \frac{(\overline{OO^*})_y}{R} \right) \tag{C13a}$$

Equation (C1a) then allows solution for  $\left(\frac{p}{R}\right)$  :

$$\left(\frac{p}{R}\right) = \frac{1}{b_{1x}} (\cos\gamma - 1) \tag{C13b}$$

and equation (25c) provides:

$$\left(\frac{Z}{R}\right) = (\cos\gamma - 1) \frac{b_{1z}}{b_{1x}} \tag{C13c}$$

In the main body of the paper,  $\gamma$  and the instantaneous cross-sensitivity, from equation (C7), are plotted as a continuous function of normalised time but here, in Table C4, they are shown for illustrative purposes just at instantaneous y-radial displacements of  $(\overline{OO^*})_y = \pm 0.01R$  and  $\pm 0.1R$ .

**Table C4**

Instantaneous solutions to equations (25a-c) and calculation of instantaneous cross-sensitivity for scenario 4 (angle of incidence 15°).

$\frac{(\overline{OO^*})_y}{R}$	$\left(\frac{p}{R}\right)$	$\gamma(\text{mrad})$	$\left(\frac{Z}{R}\right)$	Cross-sensitivity %
0.01	0.00005177	-10.00	-0.00001340	-1.00
-0.01	0.00005177	10.00	-0.00001340	1.00
0.1	0.005189	-100.17	-0.001343	-9.95
-0.1	0.005189	100.17	-0.001343	9.95

**Data availability**

Data will be made available on request.

**References**

- [1] E. Downham, R. Woods, The rationale of monitoring vibration on rotating machinery in continuously operating process plant, *Trans. ASME J. Eng. Ind.* (1971) 71-Vibr-96.
- [2] R.B. Randall, State of the art in monitoring rotating machinery - Part 1, *Sound Vibrat.* 38 (3) (2004) 14–21. <http://www.sandv.com/downloads/0403rand.pdf>.
- [3] M. Tiboni, C. Remino, R. Bussola, C. Amici, A review on vibration-based condition monitoring of rotating machinery, *Appl. Sci.* 12 (3) (2022) 972–1015, <https://doi.org/10.3390/app12030972>.
- [4] S. Doshi, A. Katoch, A. Suresh, F.A. Razak, S. Datta, S. Madhavan, C.M. Zanhari, E. Gundabattini, A review on vibrations in various turbomachines such as fans, compressors, turbines and pumps, *J. Vib. Eng. Technol.* 9 (2021) 1557–1575, <https://doi.org/10.1007/s42417-021-00313-x>.
- [5] S. Rothberg, M.S. Allen, P. Castellini, D. Di Maio, J.J.J. Dirckx, D.J. Ewins, B. Halkon, P. Muyshondt, N. Paone, T. Ryan, H. Steger, E.P. Tomasini, S. Vanlanduit, J.F. Vignola, An international review of laser Doppler vibrometry: making light work of vibration measurement, *Opt. Lasers Eng.* 99 (2017) 11–22, <https://doi.org/10.1016/j.optlaseng.2016.10.023>.
- [6] S.J. Rothberg, M. Tirabassi, A universal framework for modelling measured velocity in laser vibrometry with applications, *Mech. Syst. Sig. Process.* 26 (2012) 141–166, <https://doi.org/10.1016/j.ymssp.2011.06.022>.
- [7] S.J. Rothberg, B.J. Halkon, M. Tirabassi, C. Pusey, Radial vibration measurements directly from rotors using laser vibrometry: The effects of surface roughness, instrument misalignments and pseudo-vibration, *Mech. Syst. Sig. Process.* 33 (2012) 109–131, <https://doi.org/10.1016/j.ymssp.2012.06.011>.
- [8] B.J. Halkon, S.J. Rothberg, Angular (pitch and yaw) vibration measurements directly from rotors using laser vibrometry, *Mech. Syst. Sig. Process.* 46 (2) (2014) 344–360, <https://doi.org/10.1016/j.ymssp.2014.01.013>.

- [9] H. Khalil, D. Kim, Y. Jo, K. Park, Optical derotator alignment using image-processing algorithm for tracking laser vibrometer measurements of rotating objects, *Rev. Sci. Instrum.* 88 (2017) 065111, <https://doi.org/10.1063/1.4984125>.
- [10] B. Altmann, T. Betker, C. Pape, E. Reithmeier, Alignment strategy for an optomechanical image derotator using a laser Doppler vibrometer, *Appl. Opt.* 58 (24) (2019) 6555–6568, <https://doi.org/10.1364/AO.58.006555>.
- [11] R. Atashkhoeei, J.C. Urresti, S. Royo, J.R. Riba, L. Romeral, Runout tracking in electric motors using self-mixing interferometry, *IEEE/ASME Trans. Mechatron.* 19 (1) (2012) 184–190, <https://doi.org/10.1109/TMECH.2012.2226739>.
- [12] A.J. Oberholster, P.S. Heyns, A study of radial-flow turbomachinery blade vibration measurements using Eulerian laser Doppler vibrometry, In *AIP Conference Proceedings* 1600 (1) (2014) 23–32, <https://doi.org/10.1063/1.4879565>.
- [13] K. Tatar, P. Gren, Estimation of the in-plane vibrations of a rotating spindle, using out-of-plane laser vibrometry measurements, *Mech. Syst. Sig. Process.* 72 (2016) 660–666, <https://doi.org/10.1016/j.ymssp.2015.11.023>.
- [14] Y. Xiu-kun, T. Xiao-qi, M.A. Guo-lu, Real-time monitoring of the flexural and torsional vibration of the main axle of a numerically-controlled machine tool, *J. Opt.* 46 (2017) 352–357, <https://doi.org/10.1007/s12596-016-0385-7>.
- [15] M. Béres, B. Paripás, Measuring of drill bit vibration by laser Doppler methods, In *IOP Conf. Ser.: Mater. Sci. Eng.* 448 (1) (2018) 012068, <https://doi.org/10.1088/1757-899X/448/1/012068>.
- [16] S.J. Rothberg, N.A. Halliwell, Vibration measurements on rotating machinery using laser Doppler velocimetry, *Trans. ASME J. Vib. Acoust.* 116 (1994) 326–331, <https://doi.org/10.1115/1.2930432>.
- [17] J.R. Bell, S.J. Rothberg, Laser vibrometers and contacting transducers, target rotation and six degree-of-freedom vibration: what do we really measure? *J. Sound Vib.* 237 (2) (2000) 245–261, <https://doi.org/10.1006/jsvi.2000.3053>.
- [18] B.J. Halkon, S.J. Rothberg, Rotor vibration measurements using laser Doppler vibrometry; essential post-processing for resolution of radial and pitch / yaw vibrations, *Trans. ASME, J. Vib. Acoust.* 128 (2006) 8–20, <https://doi.org/10.1115/1.2149389>.
- [19] K. Tatar, M. Rantatalo, P. Gren, Laser vibrometry measurements of an optically smooth rotating spindle, *Mech. Syst. Sig. Process.* 21 (4) (2007) 1739–1745, <https://doi.org/10.1016/j.ymssp.2006.08.006>.
- [20] K. Agusanto, G. Lau, T. Liu, C. Zhu, Effect of oblique retroreflection from a vibrating mirror on laser Doppler shift, *Appl. Opt.* 58 (2019) 2277–2283, <https://doi.org/10.1364/AO.58.002277>.
- [21] K. Agusanto, G.K. Lau, T. Liu, C. Zhu, Radial and tangential velocity effects of a probed scanning mirror on laser Doppler frequency shift, *Appl. Opt.* 59 (12) (2020) 3792–3798, <https://doi.org/10.1364/AO.387267>.
- [22] H.R. Harrison, T. Nettleton, *Advanced Engineering Dynamics*, Arnold, London, 1997.